Stony Brook University

Cooling and Trapping of Rubidium and Francium Ions in a Linear Radio-Frequency Quadrupole Trap

A Dissertation Presented

by

Kerim Gulyuz

to

The Graduate School

in Partial Fulfillment of the Requirements

for the Degree of

Doctor of Philosophy

in

Physics

Stony Brook University

December 2007

Stony Brook University

The Graduate School

Kerim Gulyuz

We, the dissertation committee for the above candidate for the Doctor of Philosophy degree, hereby recommend acceptance of the dissertation.

Gene D. Sprouse - Dissertation Advisor
Distinguished Professor, Department of Physics and Astronomy

Linwood L. Lee - Chairperson of Defense
Professor, Department of Physics and Astronomy

Philip B. Allen
Professor, Department of Physics and Astronomy

Roy A. Lacey
Professor, Department of Chemistry

This dissertation is accepted by the Graduate School.

Lawrence Martin
Dean of the Graduate School

Abstract of the Dissertation
Cooling and Trapping of Rubidium and Francium Ions in a Linear Radio-Frequency Quadrupole Trap

by

Kerim Gulyuz

Doctor of Philosophy

in

Physics

Stony Brook University

2007

Charged particles can be confined using electromagnetic fields in an ion trap. Ions, which are essentially at rest in the trap, provide a sample for high-precision experiments. Two linear radio-frequency quadrupole (RFQ) traps have been developed to cool and confine the ions in preparation for a nuclear g-factor measurement in Francium isotopes.

The radioactive Francium is produced in a nuclear reaction using the Stony Brook superconducting LINAC. Polarization and collinear spectroscopy measurements have been performed on atomic beams. The first of the developed traps is used to cool, confine and finally extract the ions in bunches into a shorter second trap which is used to catch the ion bunches and collect them for extended periods of time. Various aspects of cooling and RFQ confinement

processes are studied with Rubidium and Francium ions.

Nuclear g-factor measurements are planned with polarized and trapped Francium isotopes. Such measurements would be an important step in preparation of a parity non-conservation experiment.

To Mehtap and my family

Contents

List of Figures

List of Tables

Acknowledgements

I would like to express my gratitude to the people who made it possible to perform the experiments presented in this dissertation.

Above all, I must mention my advisor, Prof. Gene D. Sprouse, who was always helpful, friendly and patient. I am very thankful to him for being an excellent advisor. My partner in this experiment, Jerry Sell, also deserves many thanks. We joined the experiment at the same time, and it was a pleasure working with him.

I also thank the Nuclear Structure Laboratory staff; Rich Lefferts, Bruce Gutschow, and Andrej Lipski for all their support. I would also like to thank Pat Peiliker and Socoro Delquaglio for providing friendly administrative support. Walter Schmeling and Jeff Slechta of the machine shop were very helpful in bringing the drawings to the real life.

I would like to thank also all my roommates; Ibrahim Unal, Selcuk Eren, Mustafa Kalafat, Cem Kuscu and Caner Koca with whom I have enjoyed an atmosphere full of fun during my time as a graduate student. I am also grateful to my friends; Sadri Altinok, Yuksel Kilic, Mustafa Findikci, Doga Gunay, Atilla Kaya, and Alparslan Buyukbayraktar.

Finally, I would like to thank my parents, Salih and Sebile Gulyuz, and my sister, Berrin, for their unconditional love and support. Although we were long distances apart, I have always felt their love. I would like to thank especially my wife, Mehtap, for being a great companion. This dissertation is dedicated to her and my family.

Chapter 1

Introduction

The research on francium at the Stony Brook Nuclear Structure Laboratory started with the long term goal of making parity non-conservation (PNC) measurements in francium isotopes, to better understand the weak interaction parameters. PNC experiments in Cs [1, 2] have been successful in terms of their sensitivity in measurements, and provided a new vision for weak interaction studies within the nucleus. With the help of *ab initio* atomic physics calculations in Cs [3, 4], measurements could set some constraints on the physics beyond the Standard Model [5], and indicate an extra Z' neutral gauge boson similar to those predicted in a class of superstring theories [6]. These exciting developments motivate similar sensitive measurements on francium, for which the PNC effects are predicted to be 18 times larger than for Cs [7]. Considering that the weak interaction studies require precision measurements, the importance of Fr becomes clearer. This dissertation is about the development of an experimental system to make precise measurements on a related quantity, the

nuclear g-factor of trapped francium ions. Before going into the details of the planned measurement, it is useful to give some information on Fr.

Francium, as the heaviest of the alkali atoms, has a relatively simple electronic structure which makes it a good candidate to study weak interactions. Francium was discovered by Marguerite Perey in 1939 [8], and the first optical transition was observed at CERN in 1978 [9]. In particular, not many experiments were done towards the measurement of the nuclear magnetic moments of francium isotopes. The only naturally occurring isotope, ^{223}Fr, has a half-life of 21.8 minutes. It results from the alpha decay of actinium-227 in the decay chain of ^{235}U. It is calculated that only about 30 grams of francium is present in Earth's crust at any time [10], making it the second rarest element after astatine ($_{85}$At). This natural rarity of francium is one of the reasons why it is the least studied alkali.

Experiments with Fr require production of it either, as a daughter nucleus in radioactive decay, or in a nuclear fusion reaction. These processes usually leave Fr embedded in a sample. The produced Fr must be quickly and efficiently extracted from the sample because of its short lifetime and limited abundance. The groups at Boulder/Lawrence Berkeley [11] and Moscow [12] have produced Fr from the decay of ^{229}Th with intensities of about $10^3 - 10^4$ Fr/sec.

At Stony Brook, Fr is created in a nuclear fusion reaction of oxygen on gold. The oxygen ions are accelerated to $\sim 100MeV$ using the Nuclear Structure Laboratory's tandem Van de Graaff and superconducting linear accelerator (LINAC). $^{16-18}$O ions collide with a gold target producing Fr in intensities

of $\sim 10^6$ Fr/sec. Francium trapping experiments at Stony Brook began in 1995 with successful trapping of about 1000 ^{210}Fr atoms in a magneto-optical trap (MOT) [13]. A trap with ~ 250000 ^{210}Fr in a MOT has been achieved since then [14]. The main focus of these MOT experiments was to measure the energies of some atomic transitions in Fr, lifetimes of excited states, and hyperfine splittings.

The PNC Hamiltonian in electron-nucleon interaction has two parts; the nuclear spin-independent part and nuclear spin-dependent part. It can be written as [15]

$$H_{PNC} = H_{NSI} + H_{NSD} = \frac{G_F}{\sqrt{2}}(-\frac{Q_w}{2}\gamma_5 + \frac{\kappa}{I}\boldsymbol{\alpha}\cdot\mathbf{I})\rho(r) \tag{1.1}$$

where $G_F = 10^{-5}m_p^{-2}$ is the Fermi constant, m_p is the proton mass, Q_w is the weak nuclear charge, κ is a dimensionless coupling constant, $\boldsymbol{\alpha}$ and γ_i are the Dirac matrices, $\mathbf{I}$ is the nuclear spin and $\rho(r)$ is nuclear density distribution. The large number of nucleons in Francium makes it a good candidate for PNC measurements because the spin independent part of the Hamiltonian scales as Z^3 [16] and the spin dependent part scales as $(Z+N)^{2/3}$ [7]. Thus the PNC effect in Francium is predicted to be 18 times larger than in Cs, as we stated earlier. Let us now discuss the importance of a precise g-factor measurement in Fr.

In an atomic PNC experiment, one measures the rate of an electric dipole transition between levels of the same parity. In Cs, the Boulder group has used this measured rate to determine the product of the weak matrix element, γ_5, with the weak nuclear charge [2]. To be able to determine the weak charge

Q_w, one has to calculate the weak matrix element at the nucleus from the *ab initio* theory. The matrix element depends strongly on the electron density at the nucleus as does the magnetic dipole interaction constant, A. In order to have confidence in the *ab initio* calculation of the weak matrix element, one needs to measure similar electromagnetic matrix elements that can be calculated with the *ab initio* theory. The hyperfine interaction constant, A, is essentially a product of the electron density at the nucleus $|\Psi(0)|^2$ and the nuclear g-factor. A can be measured to very high precision in atoms, including many Francium isotopes [17, 18], but the precision with which $|\Psi(0)|^2$ can be can be determined for comparison with the calculation depends on knowing the nuclear g-factor to high precision. At present, the best measurements are ± 2 %, so improving the g-factor measurements is necessary to better test the *ab initio* theory of the atom.

g-factor measurements can also make important contributions to the nuclear spin dependent part of the interaction. The hyperfine structure interaction can be written as

$$H = A\mathbf{I} \cdot \mathbf{J} \tag{1.3}$$

where A is the magnetic dipole interaction constant, $\mathbf{I}$ and $\mathbf{J}$ are the nuclear and electron spins. Bohr and Weisskopf showed that the value of the magnetic coupling strength A changes slightly from that for a point-like nucleus because of the distribution of magnetization over the nuclear volume [19]. We can express this small contribution to A as

$$A = A_p(1 + \varepsilon) \tag{1.4}$$

For a single isotope of an atom, we cannot compare precisely the measured experimental A value to A_p to extract ε, since the precision of the calculated A_p is not sufficient. So we compare the hyperfine constant of a pair of isotopes, where the uncertainties in the point-like interaction cancel, provided that the electronic wavefunction is same for both isotopes. Now we get

$$\frac{A_1}{A_2} = \frac{g_{I_1}}{g_{I_2}} \frac{(1 + \varepsilon_1)}{(1 + \varepsilon_2)} \tag{1.5}$$

where we have used $g_I = \frac{\mu_I}{I}\mu_N$, in which μ_N is the nuclear magneton. In the limit of small ε, we have

$$\frac{A_1}{A_2} \approx \frac{g_{I_1}}{g_{I_2}}(1 +^1 \Delta^2) \tag{1.6}$$

where we define: $^1\Delta^2 = \varepsilon_1 - \varepsilon_2$. Already knowing the magnetic dipole constants in some Fr isotopes to high precision, the precision measurements of the nuclear g-factors will help us to calculate the hyperfine anomaly, $^1\Delta^2$, to higher precision, and will provide us information about the neutron distribution in the nucleus.

To make a nuclear g-factor measurement in francium isotopes possible, we have built the beamline shown in Figure 1.1. The idea is to collect a sample of polarized Francium ions on which the g-factor measurements will be performed. Fr atoms are produced in the gold target by a nuclear fusion reaction. After the ions are emitted from the gold surface, they get neutralized

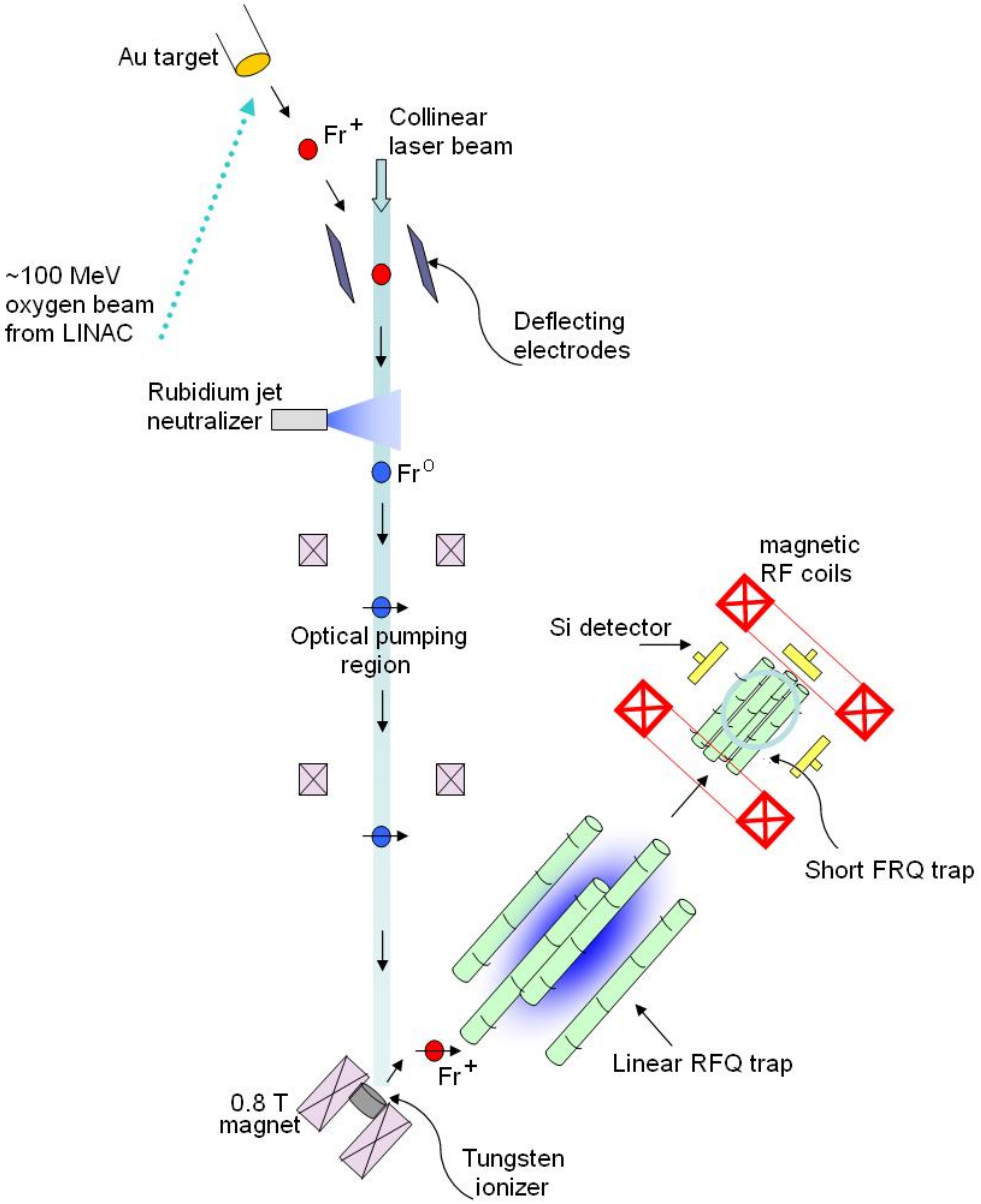

Figure 1.1: The beamline schematics for performing nuclear g-factor measurements in Francium isotopes.

by a rubidium jet, and then are polarized by optical pumping. After the neutral francium atoms land on the tungsten ionizer, they get stopped and then quickly reemitted by the hot tungsten surface. Fr leaves the surface as ions again, and the polarization is mostly preserved if the residence time of Fr on the tungsten ionizer is short [20], and they are under a strong magnetic field. The polarized ions enter the radio-frequency quadrupole (RFQ) structure, where they get slowed down by collisions with He buffer gas and eventually trapped at the bottom of a potential well, created by applying the right voltages on the trap electrodes. A weak magnetic "holding field" preserves the polarization during the process. The ions will then be released from the first trap into the shorter trap, by pulsing the relevant trap electrode voltages. The second trap, surrounded by a pair of RF coils and immersed in a uniform magnetic field, is where the nuclear g-factor measurement is planned. The RF coils will provide the necessary magnetic field to destroy the anisotropy of the polarized Fr sample. When the RF field corresponds to the Zeeman splitting, the sample will be depumped to other states, resulting in a change in the alpha decay anisotropy, which will be detected by pairs Si detectors.

The collinear laser beamline and the neutralization region are set up by my partner, Jerry Sell, and our advisor, Prof. Gene Sprouse. This section is discussed in detail in Jerry's Ph.D dissertation [21]. My work focuses on the beamline section from the W ionizer to the end of the beamline. This dissertation discusses the trapping mechanisms in both RFQ traps. Chapter 2 provides the theory for the RFQ confinement. The experimental setup for ion cooling and trapping is presented in Chapter 3. Chapter 4 contains the

computer simulations performed prior to and during the experiment. Chapter 5 studies the on-line data taking process and parameters for ion trapping. Details of the proposed nuclear g-factor measurement for future developments are explained in Chapter 6.

Chapter 2

Theory and Background

The idea of using an electromagnetic quadrupole field for ion confinement was first developed by Wolfgang Paul and his colleagues in 1953 [22]. Paul received the Nobel Prize in Physics 1989 for his work on ion traps. This chapter discusses the basic principles of dynamic ion manipulation and radio-frequency quadrupole (RFQ) traps. The equations of motion, the conditions to make a quadrupole field, and common trap types will be discussed. The discussions in this chapter closely follow the formalism of P. H. Dawson's book "Quadrupole Mass Spectrometry and its Applications (1976) [23].

2.1 Basic Principles of Ion Manipulation and Trapping

The purpose of ion manipulation using electromagnetic fields is to have control over its physical observables such as position, momentum and energy. This

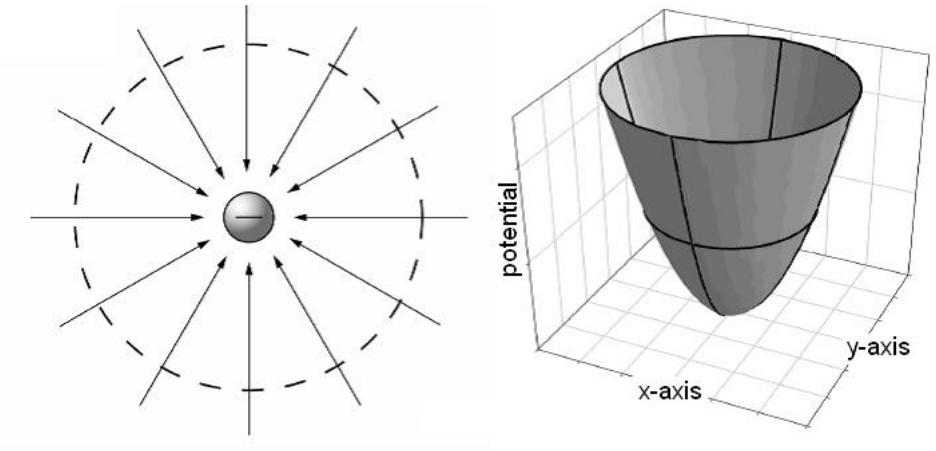

Figure 2.1: The electric field lines for a central negative charge, and the corresponding potential with the minimum at the charge center.

enables us to distinguish between different types of ions that possess different amount of charge, mass or velocity. The technique that is used in this thesis involves dynamic electric fields. But it is possible to use magnetic fields as well to make such observations of the ions.

The technique of ion manipulation relies on one of the most basic principles of physics. In an electric field, the positively charged ions are accelerated towards the lower potential and the negatively charged ones towards the higher potential. The equation of motion for an ion under an electric field is

$$m\ddot{\mathbf{x}} = e\mathbf{E} \tag{2.1}$$

where m and e are the mass and charge of the ion respectively, $\mathbf{x}$ is the position vector and $\mathbf{E}$ is the electric field vector at that position.

Figure 2.1 shows the simplest configuration for an ion trap, i.e. the case

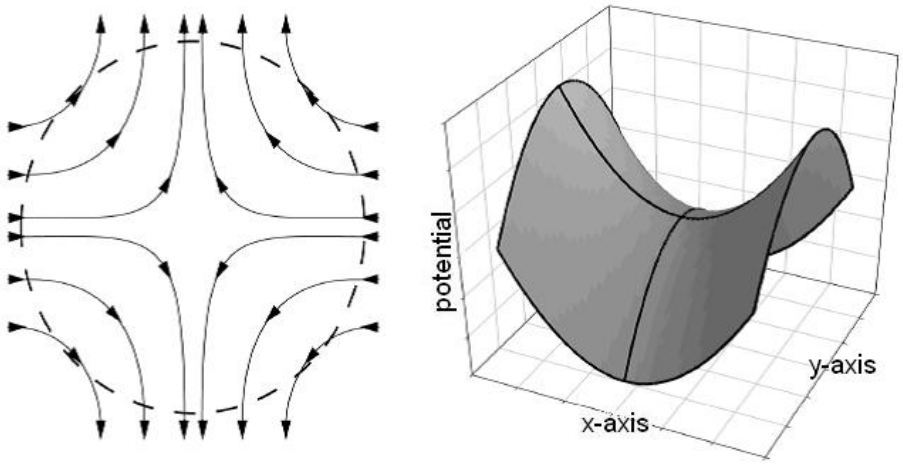

Figure 2.2: In the absence of any charge, the electric field lines entering a volume must also leave volume thus creating a minimum in one direction and a maximum in another.

where we have a charge center and all the electric field lines are radial and terminate at that center. This is a type of trap that we see in an atom. The nucleus is a potential maximum that traps negative ions.

Gauss's theorem states that for a charge configuration in free space, $\mathbf{E}$ must obey

$$\boldsymbol{\nabla} \cdot \mathbf{E} = \rho/\epsilon_0 \tag{2.2}$$

where ρ is the charge per unit volume and ϵ_0 is the permittivity of free space.

However in the absence of a charge, the electric field lines are conserved (Figure 2.2). This means any electric field lines entering a volume must also exit the volume. So it is impossible to make a potential minimum or maximum in all three directions with a static field in a vacuum. If a potential minimum is created in one spatial coordinate, then a potential maximum is also created

in at least one other coordinate.

In the absence of any charge center, Gauss's equation becomes

$$\boldsymbol{\nabla} \cdot \mathbf{E} = \mathbf{0} \tag{2.3}$$

If we express $\mathbf{E}$ as a gradient of an electric potential

$$\mathbf{E} = \boldsymbol{\nabla}\Phi \tag{2.4}$$

Then we have the Laplace's equation

$$\boldsymbol{\nabla}^2\Phi = 0 \tag{2.5}$$

To overcome the impossibility of making a trap by static electric fields, we can use non-static, alternating electric fields. Such an alternating field provides an alternately varying potential maximum and minimum in one coordinate. If we have a potential minimum in a coordinate, we then have a potential maximum in the coordinate orthogonal to it. After half a cycle of oscillation, we have the minimum reversed to maximum and the maximum to minimum. This situation can be achieved for quadrupole traps. Now it is time to move into the details of quadrupole ion traps.

2.2 The Quadrupole Field

In principle, any oscillating force field that is spatially non-uniform (thus having a local minimum or maximum potential) can be used to confine the ions. The simplest form of such fields is the quadrupole field which has a uniform gradient throughout its entire extent. It is linearly dependent on the coordinate position. In Cartesian coordinates

$$\mathbf{E} = E_0(\lambda x \hat{\mathbf{i}} + \sigma y \hat{\mathbf{j}} + \gamma z \hat{\mathbf{k}}) \tag{2.6}$$

where λ, σ, γ are some weighting constants and E_0 is a position-independent coefficient which may be time-independent. The motion in each coordinate is independent from the others, which simplifies our analysis. The force $e\mathbf{E}$ on the ion increases as the ion's displacement from zero increases. Assuming there is no space charge within the quadrupole field, the field obeys Laplace's equation

$$\boldsymbol{\nabla} \cdot \mathbf{E} = \mathbf{0} \tag{2.7}$$

which results in

$$\lambda + \sigma + \gamma = 0 \tag{2.8}$$

Two of the simplest solutions are

$$\lambda = -\sigma, \qquad \gamma = 0 \tag{2.9}$$

and

$$\lambda = \sigma, \qquad \gamma = -2\sigma \tag{2.10}$$

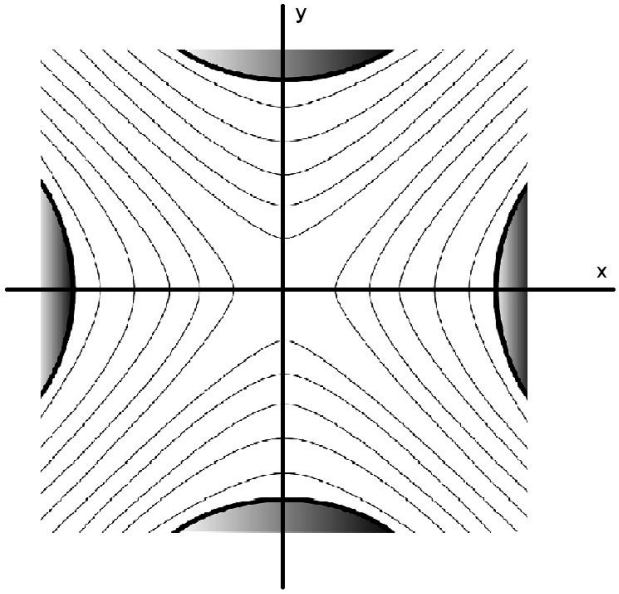

Figure 2.3: The equipotential lines for $\Phi = -\frac{E_0\lambda}{2}(x^2 - y^2)$

Because we have

$$E_x = -\frac{\partial\Phi}{\partial x}, \qquad E_y = -\frac{\partial\Phi}{\partial y}, \qquad E_z = -\frac{\partial\Phi}{\partial z} \tag{2.11}$$

integrating (2.6) gives

$$\Phi = -\frac{E_0}{2}(\lambda x^2 + \sigma y^2 + \gamma z^2) \tag{2.12}$$

The condition (2.9) above gives us

$$\Phi = -\frac{E_0\lambda}{2}(x^2 - y^2) \tag{2.13}$$

The corresponding equipotential lines are shown in Figure 2.3.

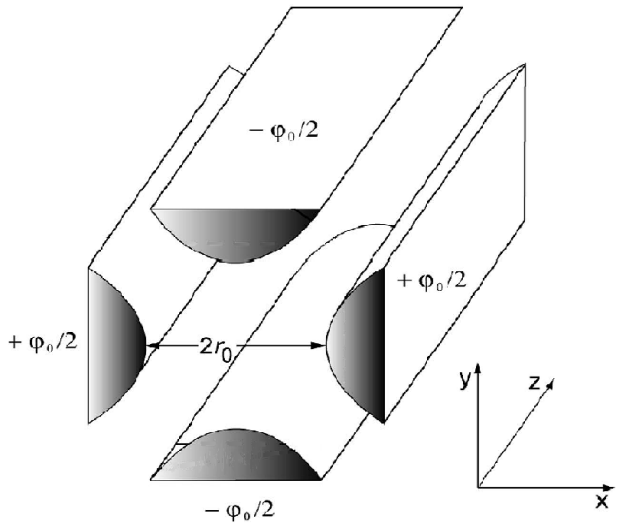

Figure 2.4: The hyperbolic structure to create a potential of the form $\Phi = -\frac{\Phi_0}{2r_0^2}(x^2 - y^2)$. The corresponding equipotential lines are shown in Figure 2.3.

We can create such a form of potential by a set of four hyperbolic cylinders with adjacent electrodes oppositely charged as in Figure 2.4. If the minimum distance between opposite rods is $2r_0$ and the potential between the neighboring electrodes is Φ_0 then (2.13) reads

$$\Phi = -\frac{\Phi_0}{2r_0^2}(x^2 - y^2) \tag{2.14}$$

The other choice of λ, σ and γ as in (2.10), i.e. $\lambda = \sigma$, $\gamma = 2\sigma$ gives us

$$\Phi = -\frac{E_0\lambda}{2}(x^2 + y^2 - 2z^2) \tag{2.15}$$

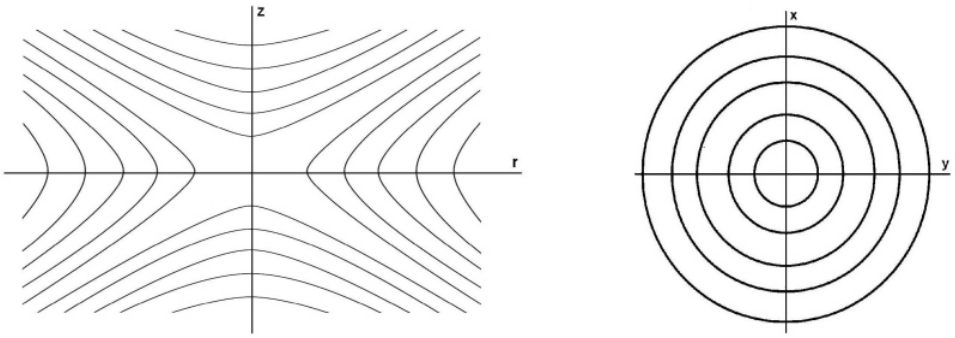

Figure 2.5: The equipotential lines for $\Phi = -\frac{E_0\lambda}{2}(r^2 - 2z^2)$

or in cylindrical coordinates

$$\Phi = -\frac{E_0\lambda}{2}(r^2 - 2z^2) \tag{2.16}$$

The equipotential lines of the corresponding situation are shown in Figure 2.5.

This form of potential can be created by an electrode structure shown in Figure 2.6. If the potential difference between the end caps and ring electrode is Φ_0, then

$$\Phi = -\frac{\Phi_0}{2r_0^2}(r^2 - 2z^2) \tag{2.17}$$

2.3 The Form of the Applied Potential and the Equations of Motion

Our primary interest in this thesis is the quadrupole traps of linear type as in Figure 2.4 where $\lambda = -\sigma$ and $\gamma = 0$, i.e. $\Phi = -\frac{\Phi_0}{2r_0^2}(x^2 - y^2)$. The equations of

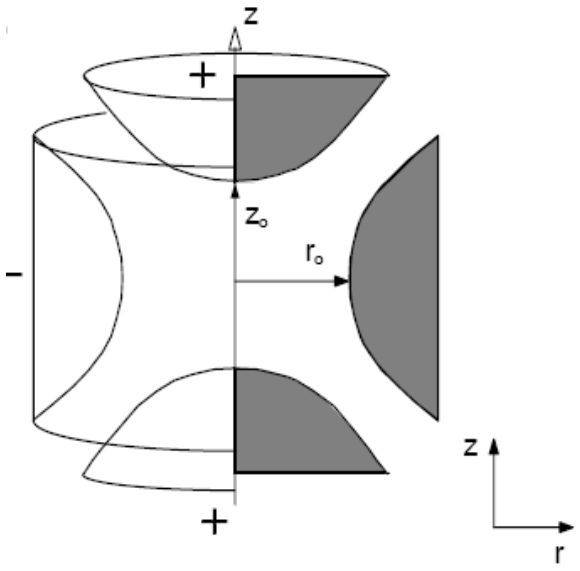

Figure 2.6: The structure to create a potential of the form $\Phi = -\frac{\Phi_0}{2r_0^2}(r^2 - 2z^2)$. The corresponding electric field lines are shown in Figure 2.5.

motion follow from

$$m\ddot{x} = eE_x, \qquad m\ddot{y} = eE_y, \qquad m\ddot{z} = eE_z \tag{2.18}$$

where $E_x = -\frac{\partial\Phi}{\partial x}, \qquad E_y = -\frac{\partial\Phi}{\partial y}, \qquad E_z = -\frac{\partial\Phi}{\partial z}$. If we consider the ions to be injected in the $\hat{\mathbf{k}}$ direction, we get

$$\ddot{x} + (\frac{e}{mr_0^2})\Phi_0 x = 0 \tag{2.19}$$

$$\ddot{y} - (\frac{e}{mr_0^2})\Phi_0 y = 0 \tag{2.20}$$

$$m\ddot{z} = 0 \tag{2.21}$$

Equations (2.19), (2.20) and (2.21) represent the motion in xz and yz planes

respectively. If we choose Φ_0 to be fixed in time, then we have a simple harmonic motion in the xz plane for any ion and all trajectories would be finite in amplitude (called stable). But for fixed Φ_0, the motion on the yz plane will be unstable and defocusing for the ions causing them to get away from the z-axis.

A clever choice of Φ_0 is that it is periodic in time. In that case, the ions will alternatively be focused and defocused in both planes. However we also need to satisfy the condition that the period is short enough or the ion's mass is large enough so that the ion does not have enough time to escape from the ion guide during the defocusing part of the cycle. This condition leads to an important design and operational property of the ion guide which will be discussed later when we consider the stability conditions.

An analogy of this stability condition is a ball in a rotating saddle. As the ball begins to roll down the lower slope, the higher slope is inverted. By proper choice of the inversion frequency the ball can be kept in the saddle.

Usually Φ_0 is chosen to be

$$\Phi_0 = U - V\cos\omega t \tag{2.22}$$

where Φ_0 consists of a DC voltage part U, and a time varying part with peak amplitude V and angular frequency ω.

The equations of motion then become

$$\begin{bmatrix} \ddot{x} \\ \ddot{y} \end{bmatrix} + \frac{e}{mr_0^2}(U - V\cos\omega t)\begin{bmatrix} x \\ -y \end{bmatrix} = 0 \tag{2.23}$$

Defining two dimensionless parameters

$$a_u = a_x = -a_y = \frac{4eU}{m\omega^2 r_0^2} \tag{2.24}$$

$$q_u = q_x = -q_y = \frac{2eV}{m\omega^2 r_0^2} \tag{2.25}$$

and introducing

$$\xi = \frac{\omega t}{2} \tag{2.26}$$

and making a change of variables, we obtain

$$\frac{d^2u}{d\xi^2} + [a_u - 2q_u \cos 2\xi] \ u = 0 \tag{2.27}$$

where u is either x or y.

2.4 The Mathieu Equation

The equation (2.27) is known as the Mathieu equation in its canonical form. The Mathieu equation is a special case of the Hill equation

$$\frac{d^2u}{d\xi^2} + [a - 2q\Psi(\xi)] \ u = 0 \quad , \qquad \Psi(\xi + \pi) = \Psi(\xi) \tag{2.28}$$

The solutions to the Mathieu equation can be expressed by

$$u = \alpha' e^{\mu\xi} \sum_{n=-\infty}^{\infty} C_{2n} \ e^{2in\xi} + \alpha'' e^{-\mu\xi} \sum_{n=-\infty}^{\infty} C_{2n} \ e^{-2in\xi} \tag{2.29}$$

where α' and α'' are integration constants which depend on initial conditions u_0 , $\dot{u}_0$and ξ_0. The constants C_{2n} and μ depend on the values of a and q but not on the initial conditions. From that we can deduce that all ions with the same a and q values for a particular coordinate direction have the same periodicity of the motion, i.e. the nature of the motion is independent of the initial conditions.

The solution (2.29) depends also on μ. When μ is finite as $\xi \to \infty$, then the solution is stable. Applied to our linear RFQ structure, this means, for an applicable stability we should have $u_{\max} < r_0$. The unstable solutions are when μ increases with no limits as $\xi \to \infty$.

μ can have four possibilities:

(i) μ is real and $\mu \neq 0$. Because of $e^{\mu\xi}$ or $e^{-\mu\xi}$ factors, the solution is unstable.

(ii) μ is purely imaginary, i.e. $\mu = i\beta$ and also β is not an integer. The solutions are stable and periodic.

(iii) μ is complex. The solutions are unstable (except $u_0 = \dot{u}_0 = 0$).

(iv) μ is purely imaginary, i.e. $\mu = im$ and also m is an integer. We have periodic but unstable solutions. The solutions are called 'Mathieu functions of integral order' and they form the boundaries in (a, q) space between stable and unstable regions. We can draw an a-q diagram to show different stability regions. The shaded regions in Figure 2.7 are the stable regions where we have bounded trajectories.

Some examples of the ion trajectories for various (a, q) values are shown in Figure 2.8.

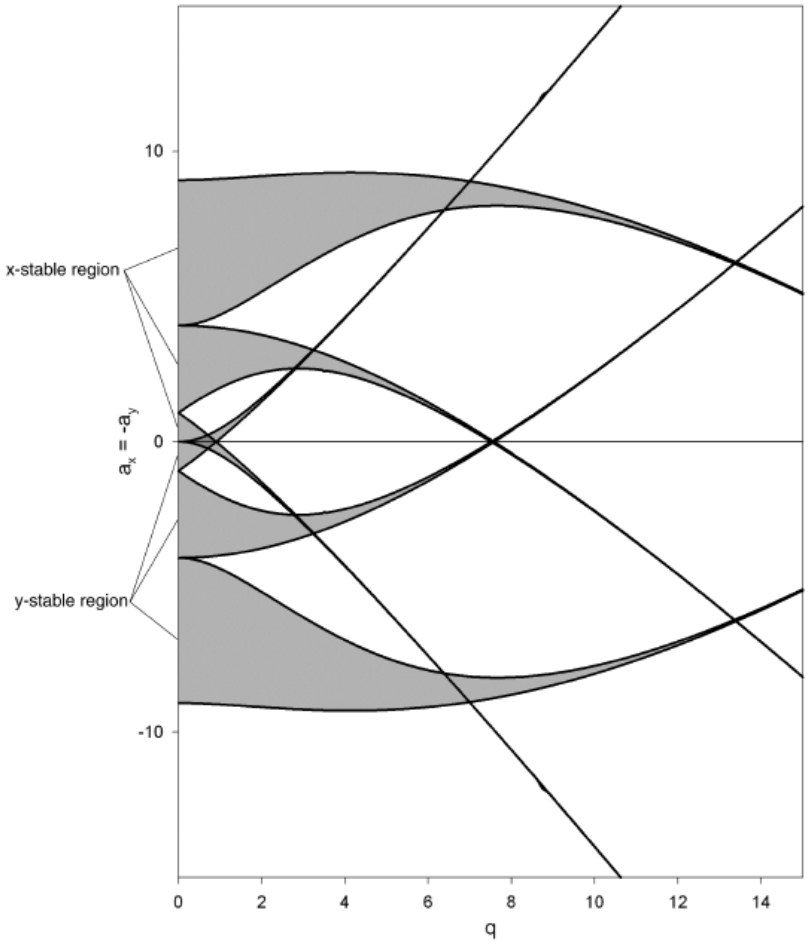

Figure 2.7: The stability regions for the ion beam guide. The motion is stable in both x and y directions when the shaded regions overlap. The first overlap on the q-axis (0<q<0.908) is called the first region of stability.

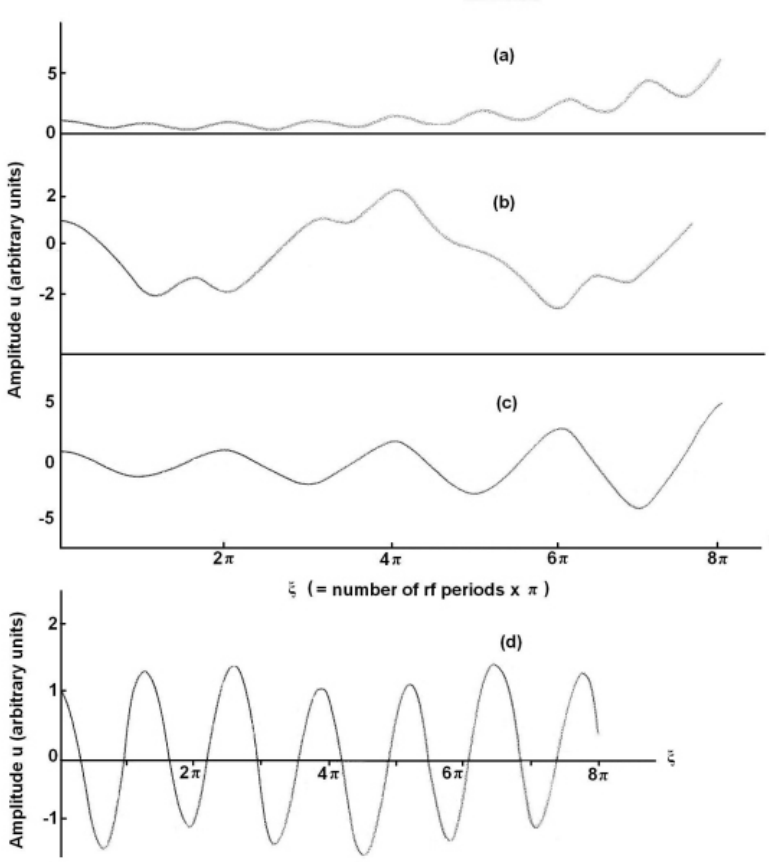

Figure 2.8: Trajectories of ions for several points in the stability diagram. (a) $q = 0.55$, $a = -0.1625$, near the lower stability limit of the first stable region; (b) $q = 0.55$, $a = 0$, within the first region of stability; (c) $q = 0.55$, $a = 0.425$, near the upper stability limit of the first stable region; (d) $q = 0.55$, $a = 2.5$, within the second region of stability. (Figure from [23])

For $\mu = i\beta$ where β is a non-integer, we can replace μ by $i\beta$ into the equation (2.29) to get

$$u = \alpha' \sum_{n=-\infty}^{\infty} C_{2n}\, e^{(2n+\beta)i\xi} + \alpha'' \sum_{n=-\infty}^{\infty} C_{2n}\, e^{-(2n+\beta)i\xi} \tag{2.30}$$

Using the identity $e^{i\theta} = \cos\theta + i\sin\theta$, we obtain the expression for stable solutions.

$$u = A \sum_{n=-\infty}^{\infty} C_{2n} \cos[(2n+\beta)\xi] + B \sum_{n=-\infty}^{\infty} C_{2n} \sin[(2n+\beta)\xi] \tag{2.31}$$

where $A = (\alpha' + \alpha'')$ and $B = i(\alpha' + \alpha'')$.

This shows that the stable solution is a superposition of oscillations with frequencies (also remember that $\xi = \frac{\omega t}{2}$ for our RFQ guide)

$$\omega_n = (2n+\beta)\frac{\omega}{2} \qquad , \qquad n = 0, 1, 2, ... \tag{2.32}$$

RFQ devices usually work in the first region of stability. A more detailed graph of the first region is shown in Figure 2.9 with iso-β contours.

The lowest term of the expansion (2.31), $n = 0$, is called the macromotion oscillation (or secular- or β-oscillation). It has the fundamental frequency of $\omega_0 = \frac{\beta\omega}{2}$. For small values of β ($\beta \leq 0.4$), it can be approximately written in terms of q.

$$\omega_0 \simeq \frac{q\omega}{\sqrt{8}} \tag{2.33}$$

We can analyze the macromotion by thinking it as an oscillation in a po-

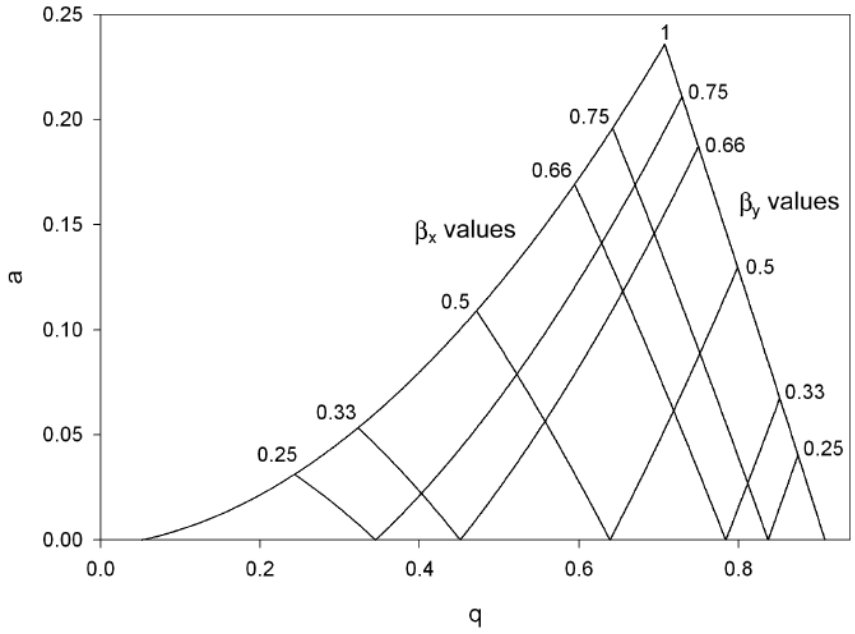

Figure 2.9: The first stability region for the Mathieu equation with iso-β curves for stable x and y values.

tential well created by the RFQ guide. Then the higher order oscillations (micromotion) can be treated as perturbations to the macromotion.

2.5 The Pseudo-potential Well

In the assumption that the sum of the higher frequency oscillations of the macromotion is small, we can express the displacement from the beam axis $\widehat{z}$ in a linear RFQ structure as the sum of two components.

$$u = \Gamma + \delta \tag{2.34}$$

where u is either x or y, Γ is a displacement due to the macromotion which describes the extent of the motion averaged over a period of the RF drive potential and δ is a small micromotion displacement resulting from the high frequency field oscillations.

If we assume that the driving force, which is related to q, is small then we can say $\delta << \Gamma$ but $\frac{d\delta}{dt} >> \frac{d\Gamma}{dt}$. By inserting these conditions into (2.27), we obtain

$$\frac{d^2\delta}{d\xi^2} = -(a_u - 2q_u \cos 2\xi)\Gamma \tag{2.35}$$

Integrating (2.35) with the assumption $a << q$ and $\Gamma = const.$, gives us

$$\delta = -\frac{q_u \Gamma}{2} \cos 2\xi \tag{2.36}$$

We immediately see that the displacement due to micromotion is out of phase

with RF potential by π and also increases linearly with the displacement Γ due to the macromotion. Now the equation (2.34) becomes

$$u = \Gamma - \frac{q_u \Gamma}{2} \cos 2\xi \tag{2.37}$$

and the equation (2.27) becomes

$$\frac{d^2u}{d\xi^2} = -a_u\Gamma + \frac{a_u q_u \Gamma}{2} \cos 2\xi + 2q_u\Gamma \cos 2\xi - q_u^2 \Gamma \cos^2 2\xi \tag{2.38}$$

Since the micromotion follows the RF frequency, the acceleration due to RF drive, $\frac{d^2\delta}{d\xi^2}$, averaged over one period of RF is zero. So we have the acceleration due to macromotion, $\frac{d^2\Gamma}{d\xi^2}$, averaged over the same period is

$$\left\langle \frac{d^2\Gamma}{d\xi^2} \right\rangle_{av.} = \frac{1}{\pi} \int_0^\pi \frac{d^2\delta}{d\xi^2} d\xi \tag{2.39}$$

Evaluating the integral by using (2.38) gives

$$\frac{d^2\Gamma}{d\xi^2} = -\left(a_u + \frac{q_u}{2}\right)\Gamma \tag{2.40}$$

or in terms of t and ω

$$\frac{d^2\Gamma}{dt^2} = -\left(a_u + \frac{q_u}{2}\right)\frac{\omega^2}{4}\Gamma \tag{2.41}$$

This is an equation of simple harmonic motion with the frequency ω_{0_u} where

we define ω_{0_u} as the macromotion oscillation frequency

$$\omega_{0_u} = \left(a_u + \frac{q_u}{2}\right)^{\frac{1}{2}} \frac{\omega}{2} \tag{2.42}$$

In the case where $a_u = 0$, i.e. when there is no DC component of the applied potential, and by substituting the expression (2.25) into (2.41) gives

$$\frac{d^2\Gamma}{dt^2} = -\left(\frac{e^2V^2}{2m^2r_o^4\omega^2}\right)\Gamma \tag{2.43}$$

The last equation is similar to the force on an ion of mass m and charge e under an electric field

$$m\frac{d^2\Gamma}{dt^2} = -e\frac{d\overline{D}_u}{d\Gamma} \tag{2.44}$$

where we call $\overline{D}_u$ as a pseudo-potential. Comparing (2.43) and (2.44) tells us

$$\frac{d\overline{D}_u}{d\Gamma} = \frac{eV^2}{2mr_0^4\omega^2}\Gamma \tag{2.45}$$

Integrating between $\Gamma = 0$ and $\Gamma = r_0$ gives

$$\overline{D}_u = \frac{eV^2}{4mr_0^2\omega^2} \tag{2.46}$$

Now we can say that for small values of q_u, the ion motion cam be expressed as an oscillating motion in a parabolic potential well in u direction (either x or y). The frequency of oscillation is equal to the fundamental macro-oscillation frequency ω_{0_u}. The total characteristics of the ion motion is a macromotion accompanied by small micro-oscillations with a phase difference of π with the

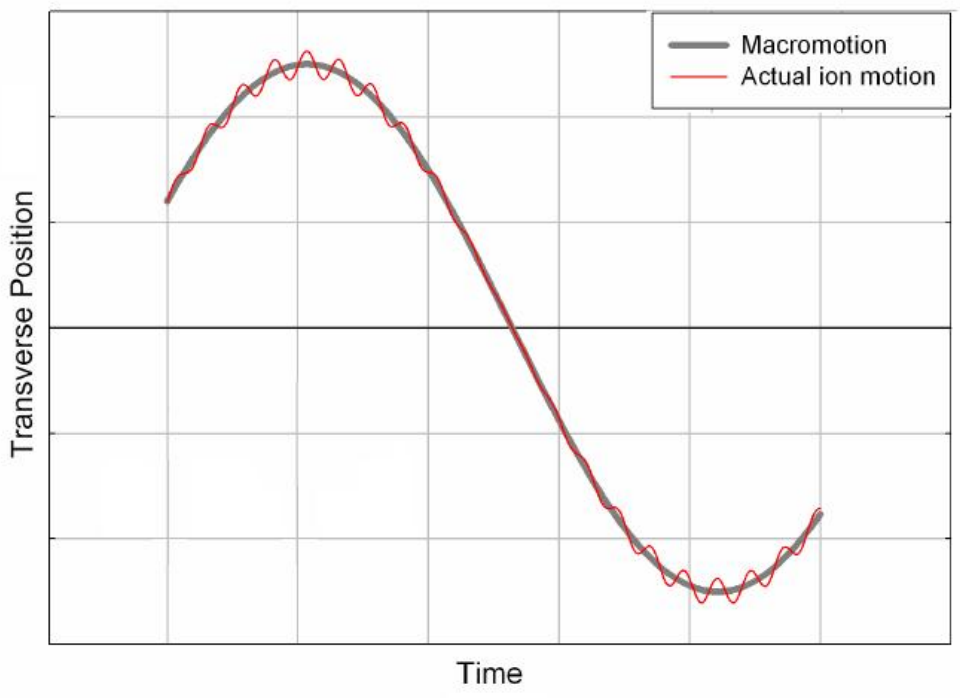

Figure 2.10: Plot of transverse position of the ion vs. time for a particular $q = 0.1$ value. The characteristics of the motion is a small micro-oscillations sitting on a simple harmonic macro-oscillation.

RF potential. The peak amplitude of the micromotion is from (2.36)

$$|\delta|_{\max} = \frac{q_u \Gamma}{2} \tag{2.47}$$

Figure 2.10 shows a plot of ion motion for $q = 0.1$.

Chapter 3

Experimental Setup for Ion Trapping

3.1 Introduction

To apply the ideas discussed in previous the chapter, we need to have a continuous supply of ions. Whether we are working with stable isotopes like Rb to test our system or we are using short-lived radio-isotopes such as francium, we have to develop a system which consists of several important sections: production, transport and trapping. Since our group is also interested in collinear spectroscopy of Rb and Fr, neutralization and re-ionization of Fr, the beamline includes regions where we perform each of the above-mentioned tasks.

A new beamline was set up to make spectroscopic and trapping measurements. Much of our time was devoted to build and debug the system. This chapter covers the design properties of the sections of our beamline, starting

from the production of francium to the trapping system.

3.2 System for Francium Production and Trapping

A diagram of our Fr beamline is given in Figure 3.1. The first region is the Fr production region. Fr is then transported through the beamline, and enters the collinear spectroscopy and neutralization region after a 10^o bend. The third region, after the W ionizer, is the trapping region.

3.2.1 Francium Production

By selecting the target, the projectile, and the beam energy, one can create nuclear fusion reactions to generate various Fr isotopes. A gold target mounted on a tungsten rod is used. ^{16}O or ^{18}O is accelerated to a beam energy of ~ 100 MeV via the Stony Brook superconducting LINAC. Such energy is enough to overcome the internuclear Coulomb barrier, and the two nuclei fuse. As a result, excess neutrons are emitted. The number of such neutrons determines the Fr isotope that remains. So the produced Francium isotope depends on the projectile isotope and the beam energy. For example, a 100 MeV ^{18}O beam hitting on a ^{197}Au target after emitting 5 neutrons mainly produces ^{210}Fr. One can optimize the production of a particular isotope by selecting the beam energy, so that the reaction cross-section for that isotope is maximum.

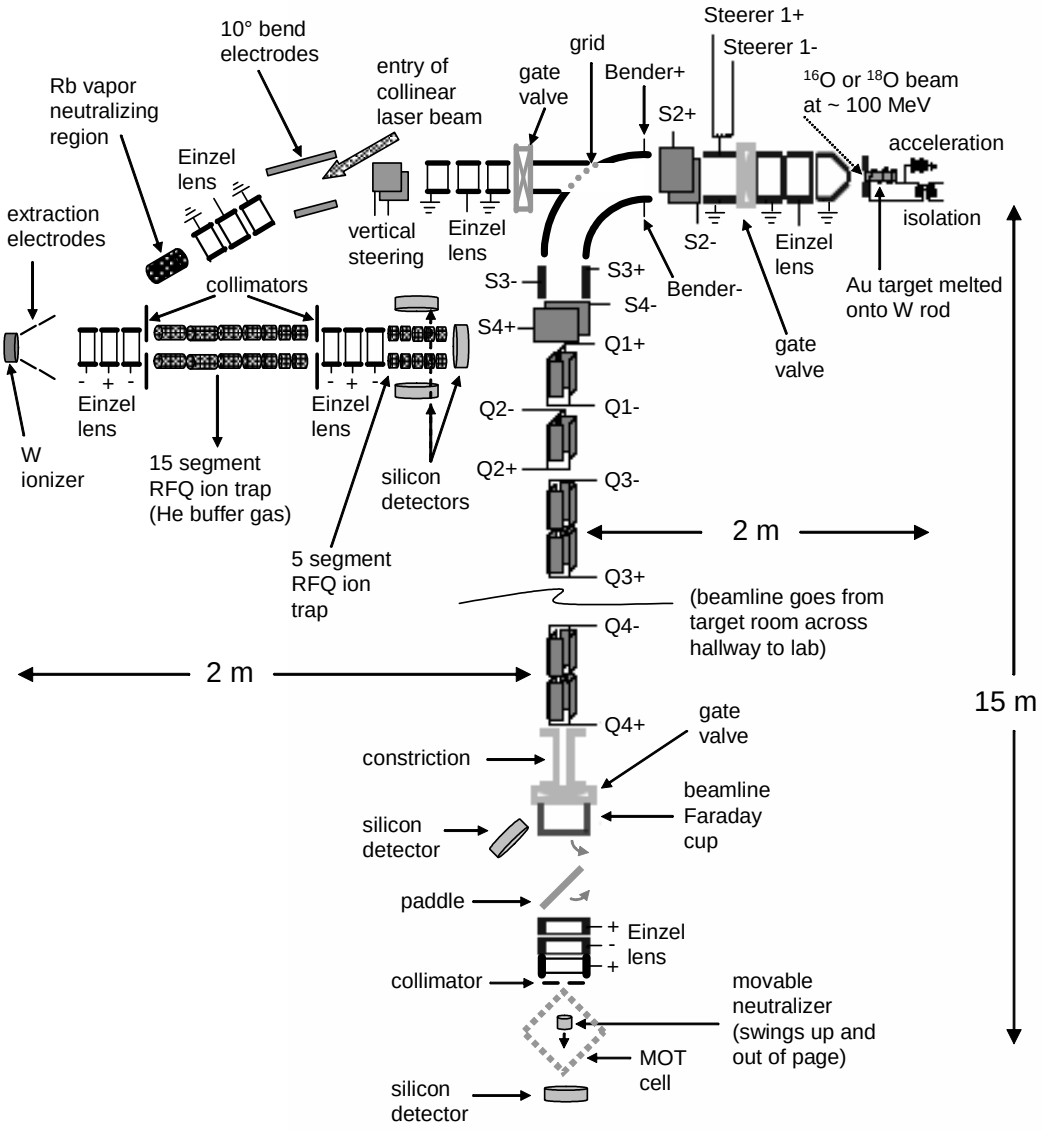

Figure 3.1: Beamline schematic for Fr ion trapping.

The production of $^{208-211}$Fr isotopes via ^{197}Au(^{18}O, xn)$^{215-x}$Fr and ^{197}Au(^{16}O, 5n)^{208}Fr is possible with our system with ^{16,18}O beam energies of 85-115 MeV.

Gold is a good candidate for target selection because of its non-reactive, mono-isotopic, chemically clean, and relatively inexpensive nature compared to separated isotopes. Our target, ^{197}Au, is melted onto the end of a 6 mm-diameter tungsten rod and flattened. The thickness of the target is usually $\sim$ 450 mg/cm^2. The oxygen beam hits the Au target at an angle of 45^o and Fr isotopes are created within the target. To make the embedded Fr diffuse to the surface easily, we bring the Au close to its melting point, T_{melt}= 1064.18 ^{o}C [8]. This is made possible by wrapping a resistive heater around the tungsten rod. Part of the heating power comes from the oxygen beam. When the target is close to its melting point, a dramatic increase in Fr release from the target is seen. The temperature of the target is monitored with a charge coupled device (CCD) camera with near-infrared sensitivity. That makes it possible to spot the location where the beam is hitting. Because of the large difference between the emissivities of liquid and solid Au, we can identify if the target is melting by just looking at the CCD camera image.

Because the work function φ of the Au target, φ(Au) = 5.1 eV, is larger than the ionization potential I_{Fr} = 4.08 eV of Fr [8], the majority of Fr evaporates from the target as ions.

To find the ratio between ions and atoms we can use the Langmuir-Saha equation [24].

$$\frac{n_t}{n_0} = \frac{w_t}{w_o} e^{\frac{\varphi - I}{kT}} \tag{3.1}$$

where n_t/ n_o is the ratio of ions to atoms desorbed. w_t/ w_o is the ratio of the

electronic partition functions which is close to $\frac{1}{2}$ for alkali atoms. Evaluating the equation for T = 1000^{o}C gives a ratio of 99.98% which means that almost all of Fr comes out as ions.

The fusion reaction, while creating Fr, generates a high neutron radiation, which forces us to set up our control system outside the target room.

For testing our system, without the complication of producing of Fr with the accelerator, we have used stable beams of ^{85}Rb or ^{87}Rb, which is obtained from a Rb dispenser strip (SAES Getters) located close to the target. The purpose of using Rb first was the fact that we can use hundreds of nanoamperes of current. The heated strip emits Rb onto the Au target where it is evaporated. The ionization potential of Rb, I_{Rb} = 4.18 eV, is also below the work function of Au, and Rb^+ behaves similar to Fr^+ in our transport system.

3.2.2 Extraction and Transport System

The purpose of the extraction and transport system is to keep the ion beam focused on the tungsten target, which is between the collinear spectroscopy and the trapping region (Figure 3.2).

The gold target is usually held at 5 kV to extract the ions. Since both Fr and Rb leave the gold surface as singly charged ions, they behave in a similar way in our transport system. The Fr production rate is too low to align the entire apparatus, so a Rb dispenser strip is used to align the beamline. The ions are guided through a set of einzel lenses and steerers to get a narrow beam at the 10^o bend where a collinear laser beam enters. It is crucial to keep the bend as small as possible, to keep the energy spread and astigmatism low.

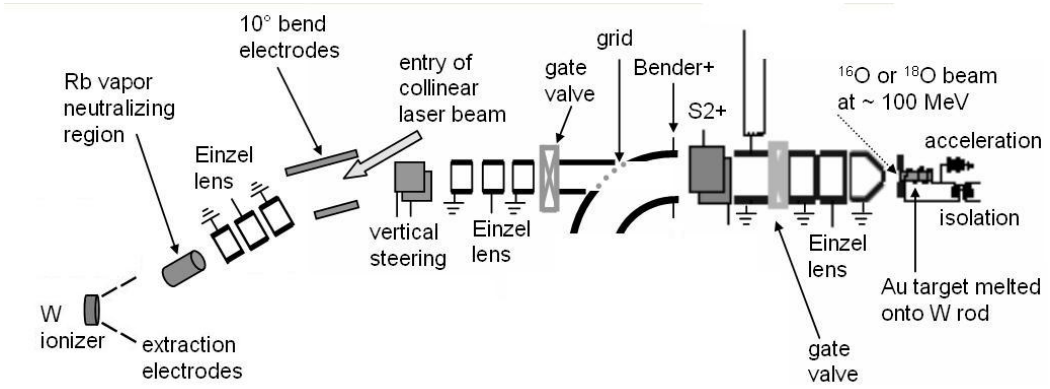

Figure 3.2: The beamline section from the Fr production (right) to tungsten taget (left). The aim is to transport the ions to the tungsten ionizer efficiently.

After another einzel lens, the ion beam enters into a Rb exchange cell, where it is converted to a neutral atomic beam by charge exchange. After that, we have a fluorescence detection region. The beam than reaches the tungsten target where it is stopped.

The tungsten heater is kept at a high temperature ($\sim 1000^oC$) to let the Fr or Rb leave the surface as an ion again. A relatively small voltage ($\sim$ 100 V) is also applied to the heater to give the ions an initial kick. Right after the tungsten heater we have a two-part cone system to shape the ions into a parallel beam (See Figure 3.3).

The beam is then focused via an einzel lens into our first trapping region, which is separated from the rest of the system with a plate which has a 6 mm-diameter hole in the center. The purpose of the small hole is to isolate the vacuum from the gas in the next section of the apparatus.

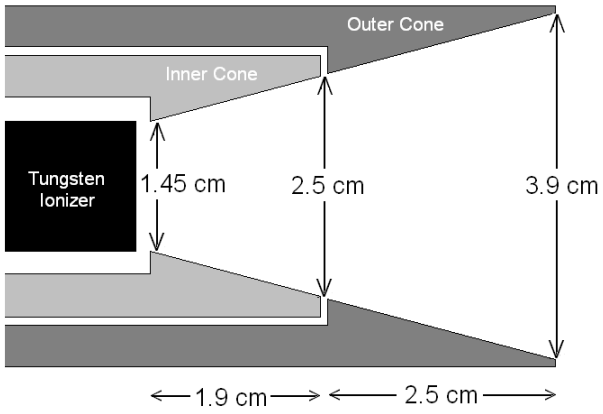

Figure 3.3: Tungsten ionizer and two-part cone system.

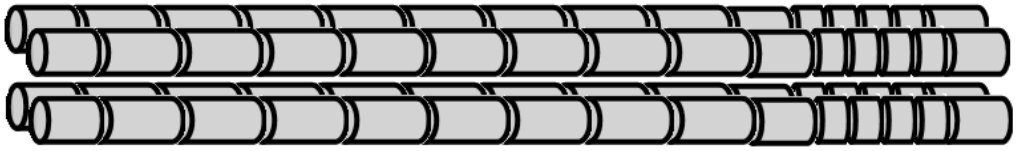

Figure 3.4: A sketch of the RFQ structure. It has 15 segments with 3 different lengths. The distance $2r_0$ between the opposite rods is selected such that the ratio (r/r_o)=1.14 where r is the radius of an electrode.

3.2.3 Radiofrequency Quadrupole (RFQ) Trap

An RFQ structure was constructed to transport and contain the ions, as shown in Figure 3.4, and by a photograph in Figure 3.5.

The structure consists of 4 parallel rods, each of which is divided into 15 segments. The purpose of the segmented rod structure is to be able to apply different DC potentials to each segment, to create a voltage gradient and a potential well along the beam direction. Each segment is isolated from its

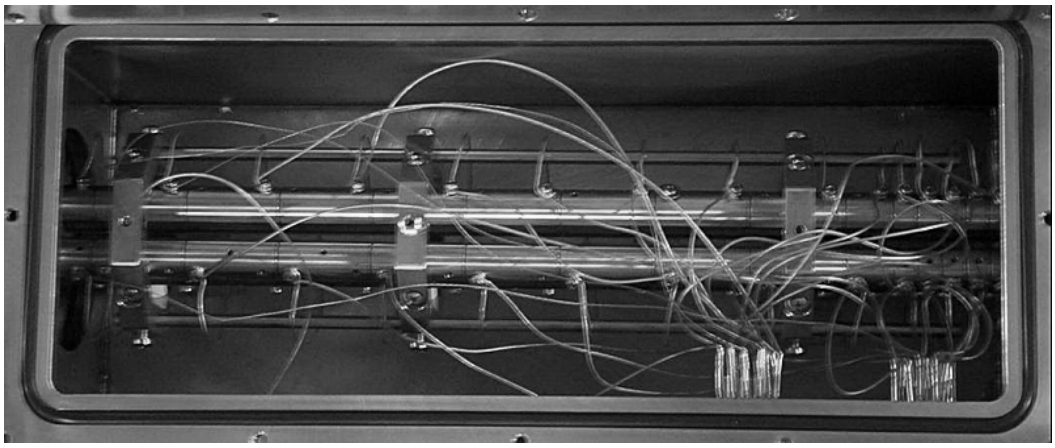

Figure 3.5: Photograph of the RFQ structure placed in trapping chamber with all its assembly and wires for electrical connections.

neighbor with glass-mica ceramic spacers, with a separation of 0.5 mm. All segments have a radius of r = 9 mm. The lengths of the segments are 4.1 cm, 2.05 cm or 1 cm, with the shorter segments being used around the trapping region.

Ideally it is best to have hyperbolic rods, but due to the difficulty in machining hyperbolic rods, circular rods are used. To imitate the hyperbolic rods with circular ones as much as possible, we have to use an optimum ratio between the radius of the circular rods and r_o, where $2r_o$ is the distance between opposite rods. That ratio is shown to be (r / r_o) = 1.148 [25, 26]. So the distance between the opposite rods is selected to be $2r_o$= 15.7 mm.

The total length of the structure is 43.65 cm. Each of the 4 rods is placed on two octagonal supports such that the parallelism and the distance between the rods is maintained. Each rod is also electrically isolated from the supporting structures with glass-mica ceramic spacers.

Each segment (60 total) has a screw hole to make an electrical connection. However we have to keep in mind, based on considerations mentioned in Chapter 2, that each opposite segment should behave in the same way. To satisfy this condition, each segment is connected carefully to its opposite pair with 16 gauge wire pieces, so that the wires do not touch any parts of the system other than the opposite pair of segments.

The RFQ structure sits in the middle section of a stainless steel rectangular box. The front section houses the last einzel lens before the RFQ structure and the connection ports to the tungsten heater assembly. The front and the middle section of the box is separated via a 3 mm thick circular plate, which has a 6 mm-diameter hole at its center, right on the beam axis. The diameter of the hole was selected based on gas flow calculations.

The middle RFQ structure section is filled with He gas to provide viscous drag via collisions between the incoming beam and the He atoms. It is necessary to keep the hole in the plate small enough so that the gas escaping from the middle section is handled by the turbopumps, located at the bottom part of the front and rear section of the box. However, the hole must be big enough to let the maximum amount of the beam inside the RFQ structure. The rear section is separated from the middle section with a similar plate, with an 8 mm-diameter hole at its center.

The distance between these plates and the first/last segments of the trap is about 5 mm. All three sections contain small ports for the necessary electrical connections and pressure gauges. The flow of He is controlled with a needle valve, while we observe the pressure at the center section. The last segment

is mainly to connect a turbopump to the system, to increase the pumping capacity. The last section also serves as partial housing to a long (44 cm) einzel lens that connects to another beampipe, which leads to a cube-shaped structure where our second trap is located. The long einzel lens is similar to the one right before the RFQ structure, except for its length. The length of front and rear electrodes of the long einzel lens is 7 cm and 5.1 cm, respectively while the central electrode is 31.8 cm long. This allows a drift region for the beam.

After the drift region, we have a spherical cube with 4.25" conflat flange ports on each of its 6 sides, as shown in Figure 3.6. The cube contains our smaller second trap, which is a short version of the first one. It has two 2.05 cm-long segments on either ends, and three 1 cm-long segments between them. The total length of this 5-segment structure is 7.3 cm. The second trap serves as a terminal place to collect the ions which are cooled and bunched in the first trap. One side of the cube is connected to the rest of the system, and one side is used to make electrical connections to the trap. The remaining 4 sides can be used to mount a multi-channel plate (MCP) and silicon detectors for α-rate measurements.

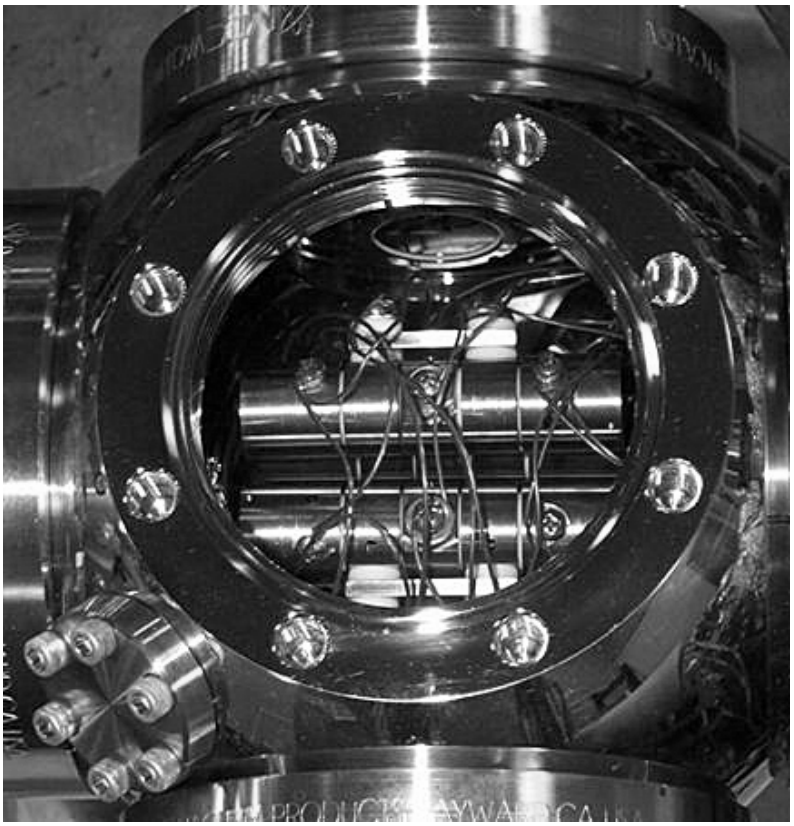

Figure 3.6: Photograph of the second trap in its housing.

Chapter 4

RFQ System Simulations with SIMION

Before building the actual parts in our system, it was crucial to demonstrate that those parts would meet our expectations. Computer simulations have been made using a program called SIMION ver.7 by D. A. Dahl from the Idaho National Laboratory [27]. The program simulates the magnetic and electric fields, for a given geometry of electrodes, in two or three dimensions. The program enables us to visualize the trajectory of ions within those fields. This gives us the flexibility of drawing all elements in our system, and to play with their shape, location in the system etc. By applying proper voltages to those electrodes in the simulation, the trajectories of the ions are visualized. In SIMION, it was also possible to define the initial conditions of the ions, such as their type, energy, charge, and initial direction of their velocities. One other possibility in SIMION is that we can add viscous drag to the ions, which

comes in handy when we simulate the effect of the collisions in the trap filled with He buffer gas. After deciding which types and shapes of electrodes to use, our goal was to determine what voltages need to be applied to them for efficient transportation of the beam, and for trapping.

The aim is to get as many ions as possible from the point of nuclear fusion between the Au target and O beam, to the point where the produced Fr gets stopped by the tungsten target. This involves selecting the acceleration voltage, having the extraction electrodes at their optimum operating voltages, and applying the right voltages to other elements such as the parallel steering plates and einzel lenses.

Once we have the ion beam well focused on the tungsten target, we are ready to simulate the rest of the system. The tungsten target is heated to $\sim 1000^0$C, to evaporate the ions back into the rest of the system. Also a positive potential is applied to the target, to repel the positively charged ions from the surface and give them an initial acceleration. This voltage was usually around 80 - 100 V during our runs. The next step was to get a parallel beam with minimum dispersion. This can be achieved by an extraction system, in our case, a two-part cone system (see Figure 3.3). By tuning the cone voltages, one can get a fairly parallel beam with an acceptable beam diameter. Several configurations of this extraction system are shown in Figures 4.1 and 4.2. Here the initial conditions for the ion beam are set such that the ions are emitted from the target at all angles, i.e. in any direction. Once we have a parallel beam, we try to focus it through the 6-mm hole that separates our cooling/trapping region from the rest of the system. The focusing is done with

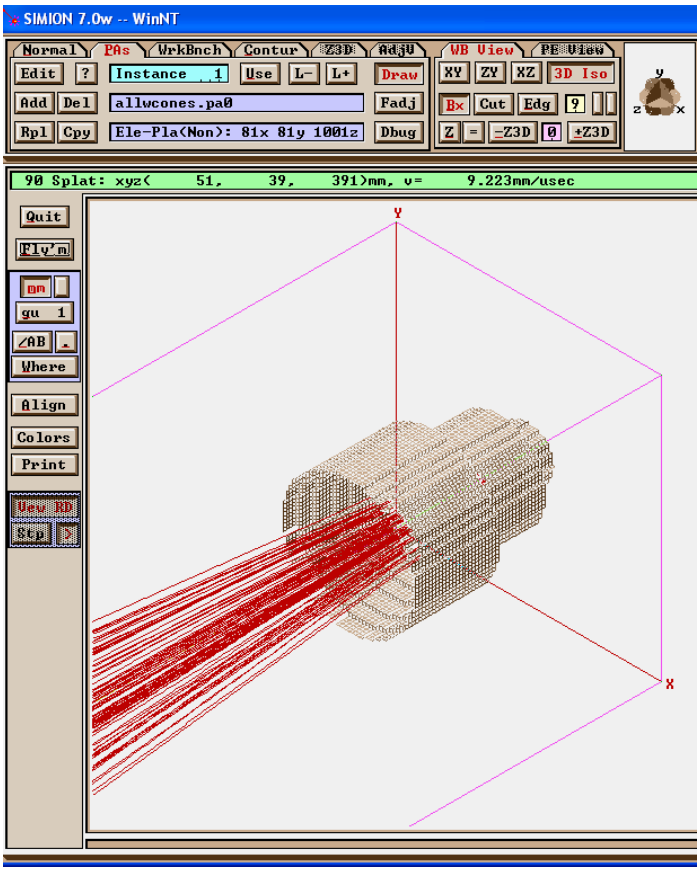

Figure 4.1: 3-D illustration of the two-cone system to extract the ions from the tunsten target. Here we have 100V on the target, 80V on the inner cone and 0 V on the outer cone.

an einzel lens (see Figure 4.3).

The focusing is successful when we have a narrow beam of ions with minimum transverse momenta. The oscillating voltage of the RFQ structure creates a pseudo-potential well which can handle ions up to a certain transverse momenum. The ions with high transverse momentum are lost by collisions to the electrodes of the structure. Once a narrow beam is obtained, we can now look at the section of our beamline where the 4-rod RFQ structure is located. This

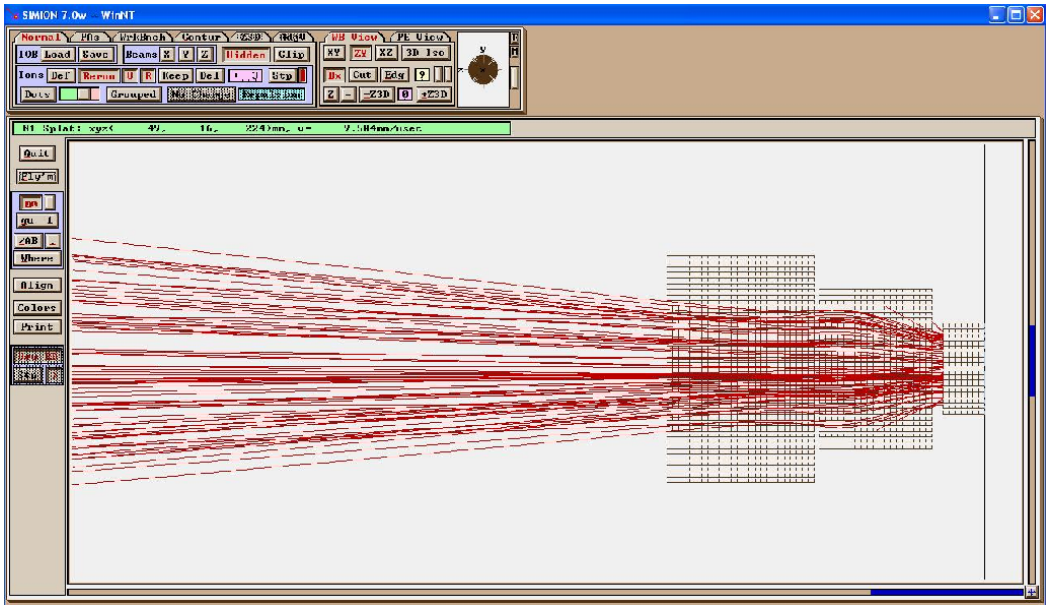

Figure 4.2: Side view of two-cone system.

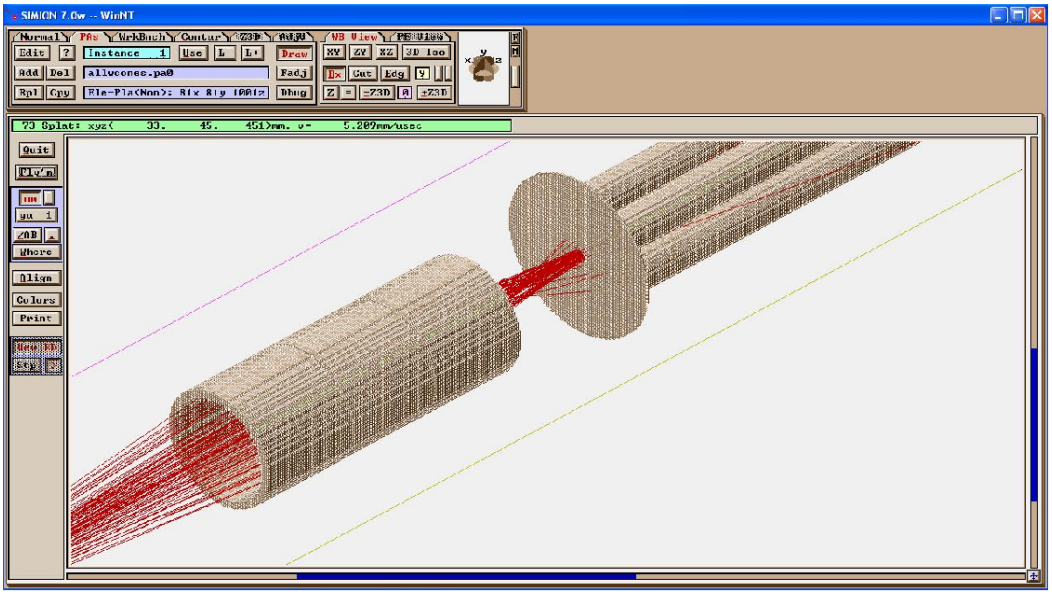

Figure 4.3: Focusing the ion beam into the trapping region through a thin hole. The diameter of the einzel lens is 50 mm, while the diameter of the hole is only 6 mm.

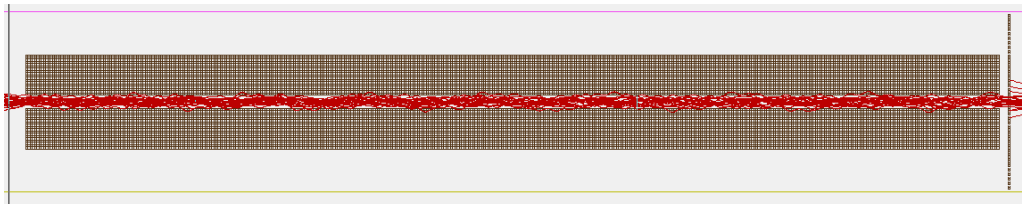

Figure 4.4: The behavious of the Fr ion beam inside the RFQ beam guide. The beam direction is from right to left and the peak-to-peak voltage on the electrodes is 300V with an oscillation frequency of 750 kHz.

section is partially isolated from the rest of the beamline *via* the two plates on both ends. When the ions enter through the 6 mm-hole, they start to feel the cooling effect of the He buffer gas. As the ions go deeper into the trapping region, they lose their kinetic energy through collisions with He atoms. This effect can be simulated in SIMION, which has the option of adding viscous drag to the ions. From the range data [28], we can enter how much energy the ions lose in a unit distance. This number can be determined for a given buffer gas pressure.

First, simulations are performed without considering the buffer gas, to enable us to see if the voltages applied to the electrodes are at their optimal values, *i.e.* if the amplitude and the frequency of the oscillating voltage are in the stability region. To see if the radial confinement is established, we can treat the RFQ beam guide as a 4-rod structure with no segments, because the segments are only useful for axial confinement. The results are shown in Figures 4.4, 4.5 and 4.6.

Next, another set of simulations has been performed with viscous drag added to the ions. The result is that they lose part of their energy and they

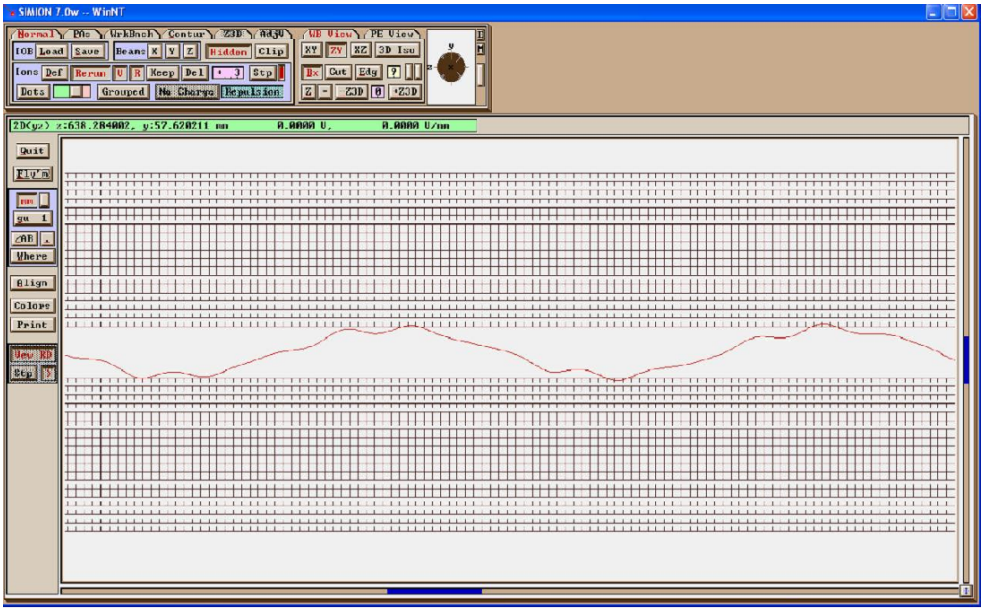

Figure 4.5: A detailed look to the trajectory of a single Fr ion in the RFQ guide. As discussed in Chapter 2, the micromotion accompanies the macromotion.

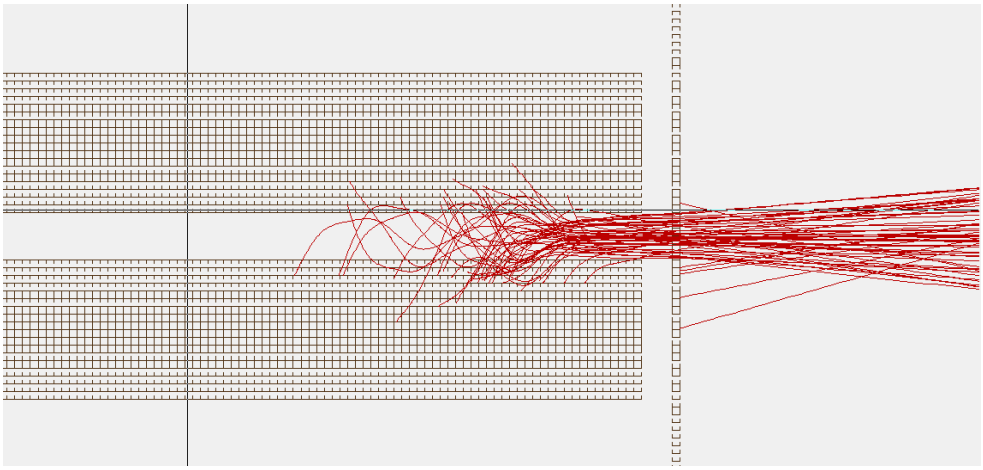

Figure 4.6: Optimal conditions for Fr ions do not work for Rb ions. As Rb enters the RFQ guide, it gets defocused and lost. So the applied voltage parameters depend on the mass of the ions. Another application of such RFQ guides is to use it as a mass spectrometer.

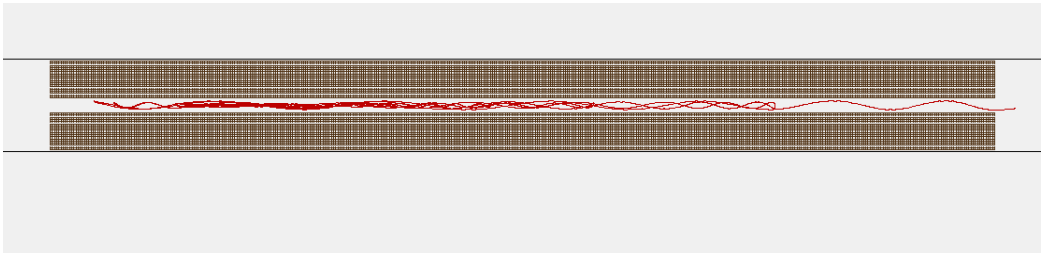

Figure 4.7: The trajectory of a sample Fr ion entering from the right side of the picture. The ion slows down by collisions with He gas and changes its direction close to the end of the trap where the potential barrier is higher than the ion's kinetic energy. The ion continues its motion until it is trapped at the bottom of the well.

are left with an energy less than the potential barrier at the end of the trap. As a result, the ions get repelled by that potential and reverse direction. The ions are now still under a viscous drag and they continue to move back and forth along the principal beam axis until they lose almost all their kinetic energy and get trapped at the bottom of the potential well. Figure 4.7 shows the trajectory of a representative Fr ion with an energy of 100eV. In Figure 4.8, we can see the ion's location along the beam axis (z) and perpendicular to the beam axis (x or y) in time.

The next set of simulations is about successful dumping of the trapped ions. The ions are now in a bunch, and they need to be sent to the second shorter trap by lowering the potential barrier at the end of the first longer trap. A successful dumping means that the ions stay in a bunch. Since they travel about 1 meter to the second trap, they should have minimum dispersion in their kinetic energy. Otherwise the front and the back of the ion bunch arrive at very different times to the second trap, making it impossible to trap them there. The long einzel lens between the two traps serves as a drift region for

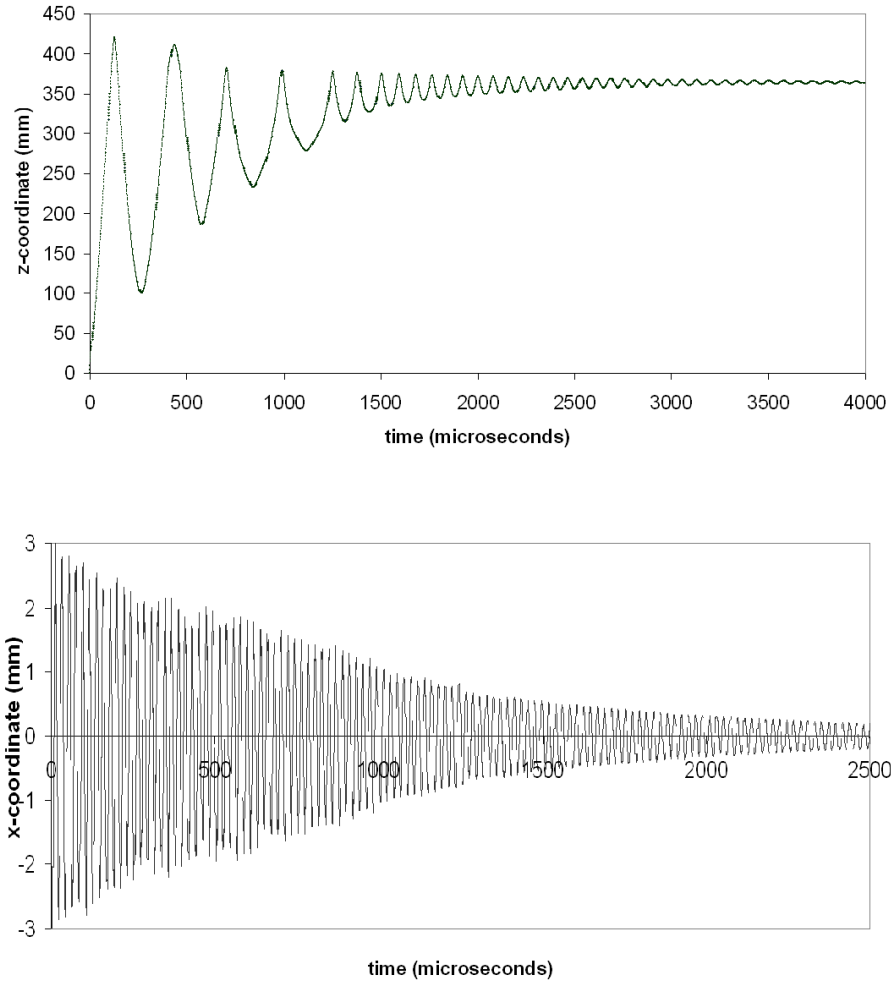

Figure 4.8: The ion's behaviour along the beam axis (z) and perpendicular to the beam axis (x) in time.

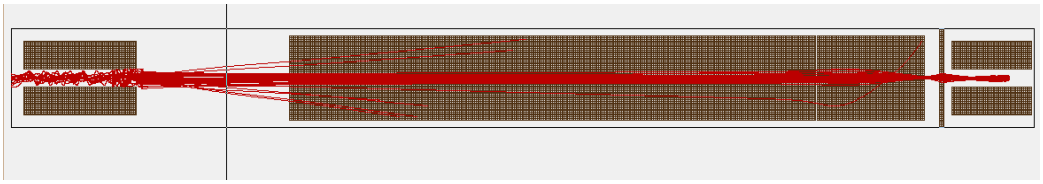

Figure 4.9: The extraction of the ion bunch from the first trap (on the right) and transferring them to the second trap (on the left) through a long einzellens.

the ion bunch, and it also allows us to focus the beam into the second trap. A simulation for the section from the first trap to the second one is shown in Figure 4.9.

After the ion bunch enters the second trap, we need to raise the voltage at the entrance of the trap so that the ion bunch stays in the trap. The entrance voltage is kept high until the subsequent bunch arrives, and the entrance voltage is lowered then again to let the next bunch in.

Simulations gave us an idea about a set of parameters such as the RF frequency, amplitude of the RF voltage, He buffer gas pressure, the depth of the potential wells created, kinetic energies and flight times of the ions, cooling time in the trap, and other electrode voltages in the system. Using those parameters, we had a good starting point for the values to be used in an on-line experiment.

Chapter 5

Radio-Frequency Quadrupole Trapping of Rubidium and Francium Ions

This chapter is about various kinds of data that have been taken with both Rubidium and Francium ions. A great deal of our effort involves testing the system with Rb because Rb is easily obtained by heating up a Rb getter foil. Running the experiment with francium requires all the complicated processes of Fr production discussed in Section 3.2.1. We determined the transfer efficiency of the ion beam for different He gas pressure, and voltage and frequency settings for successful confinement and trapping.

5.1 Selection of Operating Parameters

A good point to start with trapping is to determine whether you have control over the ion beam, *i.e.* how well can you transport the ion beam all the way from where they are emitted to where they are collected (see Figure 5.1) Our first goal was to maximize the transport to the W ionizer. The voltages on the beamline elements were adjusted such that we have a maximum beam current on the tungsten target. Between the Rb getter and tungsten target, we had a Faraday cup for further beam diagnostics. Also the two conical electrodes next to the tungsten target could be used as current measurement devices, to be able to focus the beam right on the center of the tungsten target. Once this step is achieved, we are ready to connect the tungsten target to a current source to heat it up.

5.1.1 The Efficiency of Re-emission from the Tungsten Target

To have an idea about the re-emission efficiency from the tungsten target, data have been taken with a Rb beam, because of its high available intensity compared to a Fr beam. Rb ions are initially accelerated to 5 kV. This high acceleration minimizes the losses during their way to tungsten target. When they land on the target, they get stopped and re-emitted when the tungsten is heated. During this process it is obvious that we have some losses in Rb intensity.

To find the re-emission efficiency, we have used the einzel lens and the

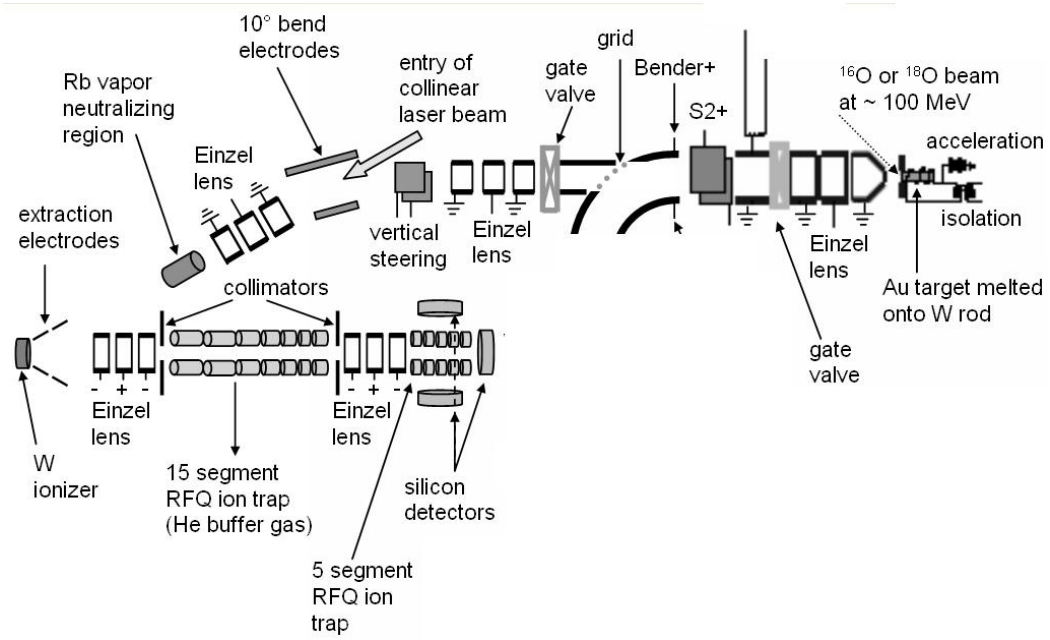

Figure 5.1: Beamline schematics form the point of emission of the ions to their final trapping region.

Heater Power (Watt)	Cup current reading (nA)	% Efficiency
19.2	2.3	15.3
21.3	2.7	18.0
23.2	2.8	18.7
25.8	2.6	17.3
28.2	2.7	18.0
31.0	3.2	21.3
33.3	3.4	22.7
35.0	3.5	23.3
38.4	3.5	23.3
41.0	3.2	21.3
43.9	3.2	21.3

Table 5.1: Tungsten ionizer power versus cup current reading. The efficiency is calculated based on the fact that 15nA of beam intensity is incident on the target initially.

plate in front of our first RFQ structure (labeled as collimator in Figure 5.1) as a big Faraday cup. First, we have measured the current on the tungsten target before heating it up. Then by applying heating power and an initial acceleration voltage on the tungsten target, we let the ions evaporate from the surface with an initial speed. The cone voltages are adjusted such that we have maximum current reading at our big Faraday cup. Table 5.1 shows the ionizer power versus the cup reading, and the respective efficiency for an initial incoming Rb ion beam of intensity of 15nA on the tungsten target.

We can deduce that around 23% of the incoming beam is reemitted by the tungsten target and sent to the big Faraday cup. The trend is: higher power leads to higher efficiency. But we do not always desire high Rb intensity coming into the RFQ structure, especially when we are running with Fr. We would like to separate Rb from Fr, and therefore we want to keep the heater power as low as possible without sacrificing much from the re-emission efficiency.

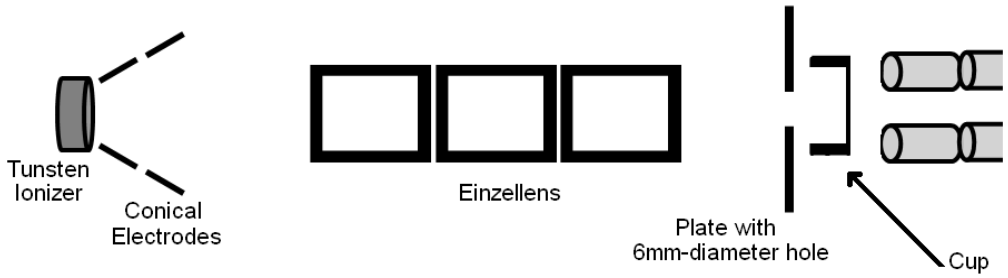

Figure 5.2: The placement of the small cup to measure the transmission efficiency into the trapping region.

5.1.2 Transport into the RFQ Structure

After the ions are reemitted from the tungsten surface, we focus them through a 6mm-diameter hole into the RFQ structure. There are elements in our system such as the tungsten target, conical electrodes, and an einzel lens, to allow us to steer the beam into the RFQ structure. First, we place a small cup right after the hole as in Figure 5.2, to measure the current into the section where our RFQ structure is located. We can use the plate in front of the cup as a collimator also.

Table 5.2 shows the applied voltages and the currents on the collimator and the cup. The data are graphed in Figure 5.3. It appears that the higher the acceleration voltage at the tungsten target, the more current is obtained at the cup. The cone and einzel lens voltages need to be adjusted in proportion with the tungsten target voltage.

However, we do not want to have the ions enter into the RFQ structure with a high kinetic energy. A higher kinetic energy beam will require higher

Ionizer Voltage(V)	Inner Cone Voltage(V)	Einzel lens Voltage(V)	Cup Current (nA)	Collimator Current (nA)
50	44	-158	78	61
100	88	-322	190	68
150	133	-490	249	47
200	175	-636	280	41
250	221	-875	303	32
300	265	-1001	325	31

Table 5.2: The voltage versus the cup current. The outer cone and the two end electrodes of the einzel lens is kept at 0 V. The inner cone and center electrode of the einzel lens is adjusted to maximize the cup current.

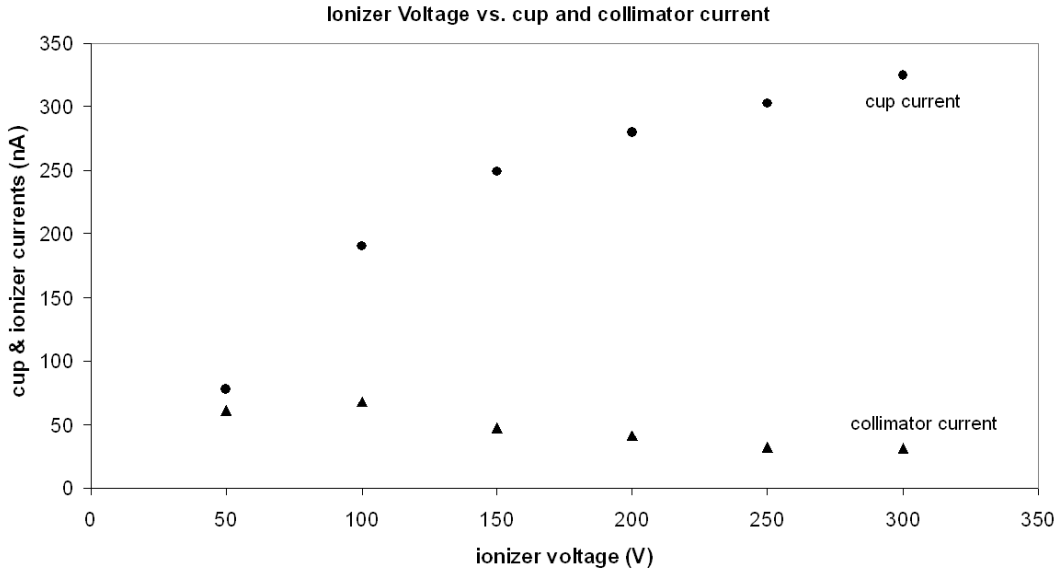

Figure 5.3: The intensity of the beam into the cup increases with increasing ionizer voltage, resulting in better focusing.

helium pressure in the trap region, to reduce the beam energy. Higher helium pressure means higher concentrations of impurities overall. We also want to keep the sections of the system, other then the trapping section, free of He as much as possible. In other words, our turbopumps must be capable of handling the He flow from the trapping region. So there is a balance between the acceleration voltage of the tungsten target and He pressure. We have selected the acceleration voltage around 100V to avoid the necessity of very high He pressure.

5.1.3 Operating Parameters of the RFQ Structure

When the ion beam enters into the section where our first RFQ trap is located, the first task is to keep the ions close to the beam axis so they do not get lost by collisions with the trap electrodes. A good point to start with, before performing any trapping experiments, is to see if we can guide the ions through the RFQ structure. All the way at the end of our experimental system (after our second trap), we set up a plate with which we can measure the rubidium current, and an alpha detector for the detection of francium ions (see figure 5.4). Because the Fr beam intensity is too low compared to the Rb intensity, the current on the plate is almost entirely Rb current. Initially, we set the oscillation frequency of the RFQ structures to f=725 kHz, which is a reasonable value for relatively heavy ions. Then we scan the RF voltage and record the Rb and Fr intensities.

A typical data set is shown in Table 5.3. A "q" value is found using equation 2.25, $q = \frac{2eV}{m\omega^2 r_0^2}$, where V is the amplitude of the RF potential applied to all

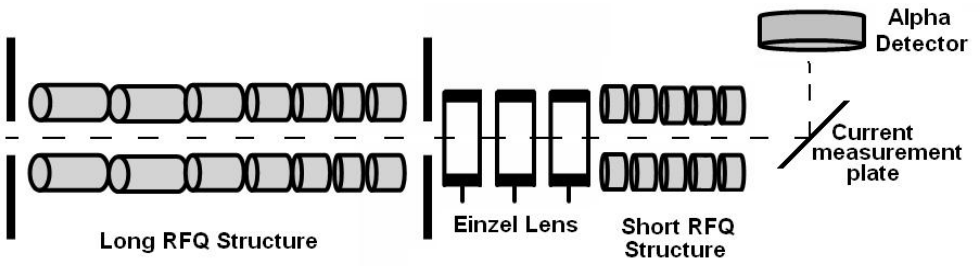

Figure 5.4: The placement of the current plate and the alpha detector to measure the transport efficiency through both RFQ structures.

the electrodes, m is the mass of the ion, and r_0 is half of the distance between the opposite rods, in our case $r_0 = 7.85mm$. A plot of the data in Table 5.3 is shown in figure 5.5. From the plot, we can deduce that Fr and Rb intensities have their maximum values at different RF voltages. They both peak when q is around 0.3 - 0.4. Comparing our results to the stability diagram in Figure 2.9, we can say that our optimal operating frequency and voltages are consistent with the theory.

5.2 Bunching and Trapping of Rubidium

After we demonstrate that we can guide the ion beam through both RFQ structures successfully, and determine the operating parameters, we are ready to try trapping the Rb^+ ions in the first linear trap. Then we can release them as an ion bunch and trap them again in the second trap. First, we start with the Rb^+ beam accelerated to 55V at the tungsten target. Then we focus the beam through the 6mm-diameter hole into the RFQ structure, by tuning the conical electrodes and einzel lens voltages. The RFQ structure operates at

RF Voltage(V)	Rb current(pA)	Fr counts(in 10s)	q for Fr	q for Rb
200	160	238	0.14	0.35
250	120	559	0.18	0.44
300	150	935	0.21	0.53
350	75	793	0.25	0.62
400	50	684	0.29	0.71
450	25	811	0.32	0.79
500	6	559	0.35	0.88
550	2.5	521	0.39	0.97
600	0.7	512	0.43	1.06
650	0.25	311	0.46	1.15
700	0.25	263	0.50	1.24
750	0.1	208	0.54	1.34
800	0.1	152	0.57	1.41

Table 5.3: The dependence of Fr and Rb transmission through the RFQ structure to the RF voltage. The data is taken at f=725 kHz.

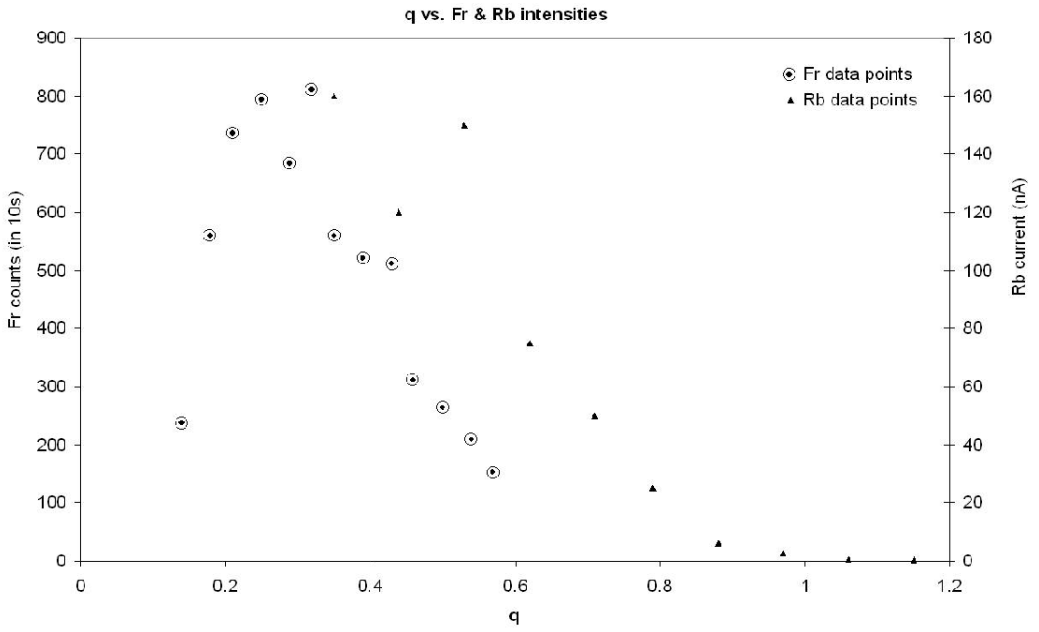

Figure 5.5: Plot of q versus Fr and Rb intensities from Table 5.3. The first stability region ends at q=0.908 beyond which the Rb intensity vanishes. Both Rb and Fr have their maxima at around q=0.3 - 0.4.

1st trap segments	DC voltage		
# 1	53.5 V	14	0 V (center of 1st trap)
# 2	46.1 V	15	95 V when collecting
# 3	45.4 V		-5V when dumping
# 4	42.6 V		
# 5	39.7 V		
# 6	36.9 V	2nd trap	
# 7	34.5 V	segments	DC voltage (V)
# 8	32.2 V	# 1	0 V when letting in
# 9	30.1 V		+100 V at other times
# 10	26.9 V	# 2	64.9 V
# 11	24.5 V	# 3	52.6 V
# 12	20.3 V	# 4	40.7 V (center of 2nd trap)
# 13	15 V when collecting +65 V when dumping	# 5	0 V when dumping out +120 V at other times

Table 5.4: Applied DC voltages to the segments of both traps. Some segments have two modes, during collection of ions and when dumping the ions

f=720 kHz and 300V of RF voltage. Also, DC potentials are applied to the trap segments to provide axial confinement (see Table 5.4). The He pressure at the first trapping region was $2.2\text{x}10^{-2}$ mbar as measured by the vacuum gauge connected to that section of the beamline.

After some Rb^+ ions are accumulated at the bottom of the DC potential well (around segment # 14), we eject them as an ion bunch from the first trap to the second trap. We use Rb at this point to show that we can successfully extract the Rb ions into the second trap, where the g-factor measurements are planned for Fr. The aim is to get a high purity ion collection in the second trap, by collecting every bunch from the first trap. Collecting several cycles of ion bunches in the second trap will enable us to get a high number of ions trapped there. To eject the ions from the first trap, we increase the DC voltage

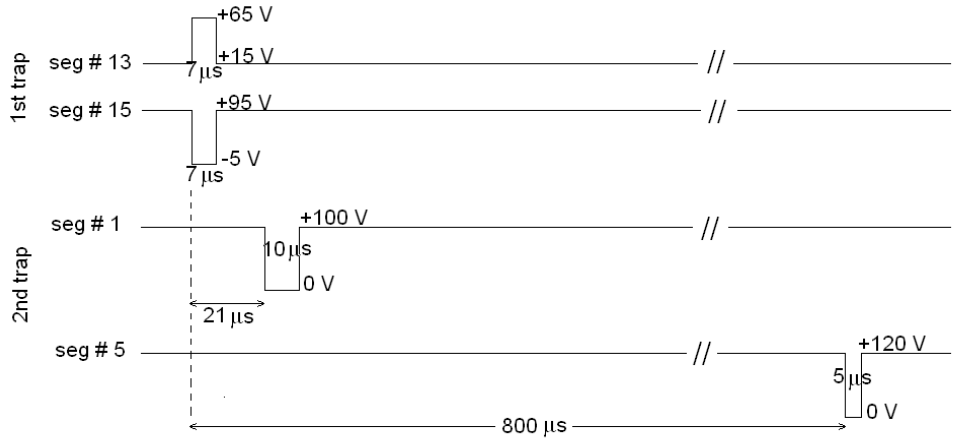

Figure 5.6: The conditions for the pulsing segments in both RFQ structures.

of the 13th segment from +15V to +65V, and decrease the DC voltage of the 15th segment and the exit plate from +95V to -5V, which gives the trapped ion beam an initial "kick" towards the second trap. The duration of the "kick" pulses are $7\mu s$. The 1st segment of the second trap is kept at +100V until the ion bunch from the first trap arrives. This time interval is $21\mu s$. Then the voltage is lowered to 0V for $10\mu s$ to let the ion bunch in. After $10\mu s$, we increase the DC voltage back to 100V.

The last (5th) segment of the second trap is kept at +120V for a relatively long period of time ($800\mu s$), to keep the ions trapped in the second trap. Then we lower its voltage to 0V relative to the pulse from the first trap, and keep the voltage low for $5\mu s$. The result is a signal at the multi-channel plate which is placed after the second trap. The signal is seen $15\mu s$ after the DC voltage of the last segment is lowered. The pulsing sequence is shown in Figure 5.6.

A picture of the MCP signal is shown in Figure 5.7. The two pulses on

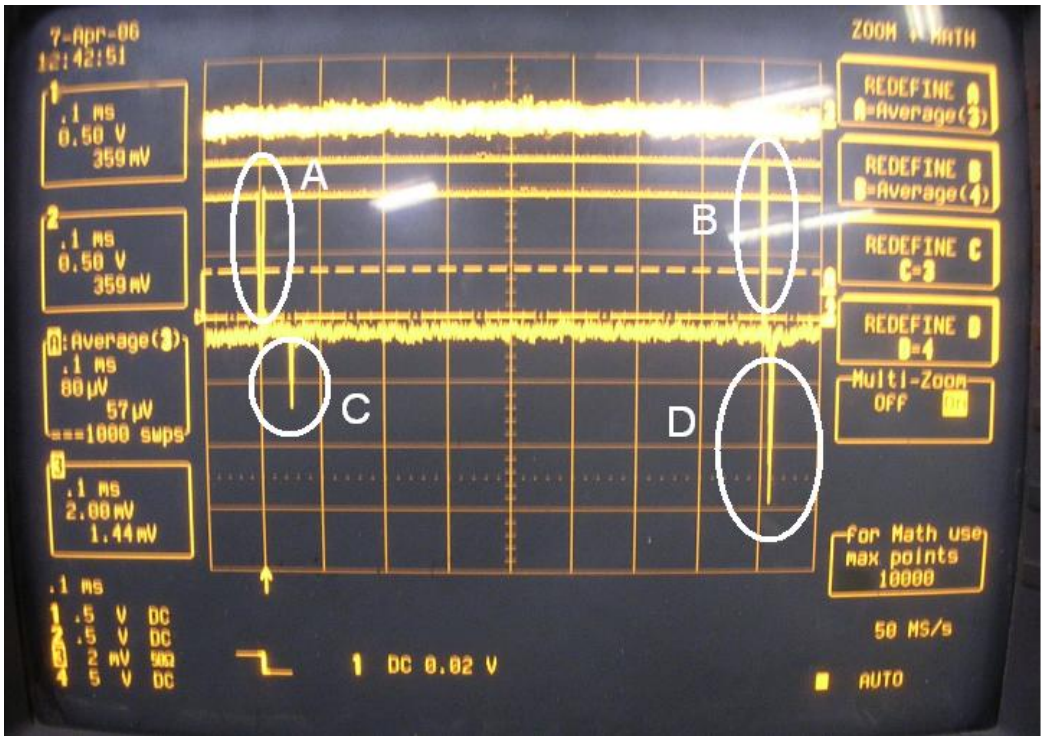

Figure 5.7: Trapping and bunching of Rb as seen from the oscilloscope screen. (A) The kick pulse of the last segment of the first trap; (B) the release pulse of the last segment of the second trap; (C) the ions that arrive to MCP untrapped after about 50 microseconds; (D) the trapped ions in the second trap arrive 15 microseconds after the DC voltage is decreased. Each horizontal time division is 0.1 ms long.

the upper half of the picture are the pulsing voltages on the segments (A & B), and the two pulses on the lower half are MCP signals. A sharp peak is apparent (D) after we drop the DC voltage at the last segment of the second trap. The smaller peak (C) is due to the part of the ion bunch that arrives at the MCP untrapped.

5.3 Trap Lifetime Calculations for Francium Ions in the First Trap

To understand the behavior of Fr^+ ions in the trap, several experiments were performed. The Fr^+ ions are created using a 100MeV ^{18}O beam on a Au target. They are then accelerated to 5kV and focused on a tungsten target as shown in Figure 5.1, where they get stopped. The tungsten target is heated to about 1000 ^0C and kept at a voltage of about +100V. The Fr^+ ions evaporate from the surface with about 100eV of kinetic energy, and we focus them with the conical electrodes and the einzel lens into the trapping region, as described earlier for Rb. Also the Rb^+ ions from our earlier experiments that are stuck on the tungsten target evaporate from the surface and get focused into the trapping region as well. But now we tune the RFQ structure settings such that only Fr^+ ions make it to the end of the RFQ structure. The segments of the RFQ structure are now operating at about 500V of RF voltage and 725 kHz of RF frequency, to maximize the Fr^+ transmission. The non-pulsing DC voltages from the 1st segment to the 12th segment decrease gradually from 80V to 25V. We keep the trap center (around 14th segment) at 0 V, and 13th segment pulses from +15V to +65V, and the 15th segment from +95V down to -5V, for a pulse duration of $8\mu s$. The ions get kicked out of the first trap as a bunch, and we detect them at our alpha detector placed after the second trap. The DC voltages at the second trap are kept at 0 V. However the RF characteristics is the same as the first trap.

At this point, we would like to see how long we can keep the Fr^+ ions

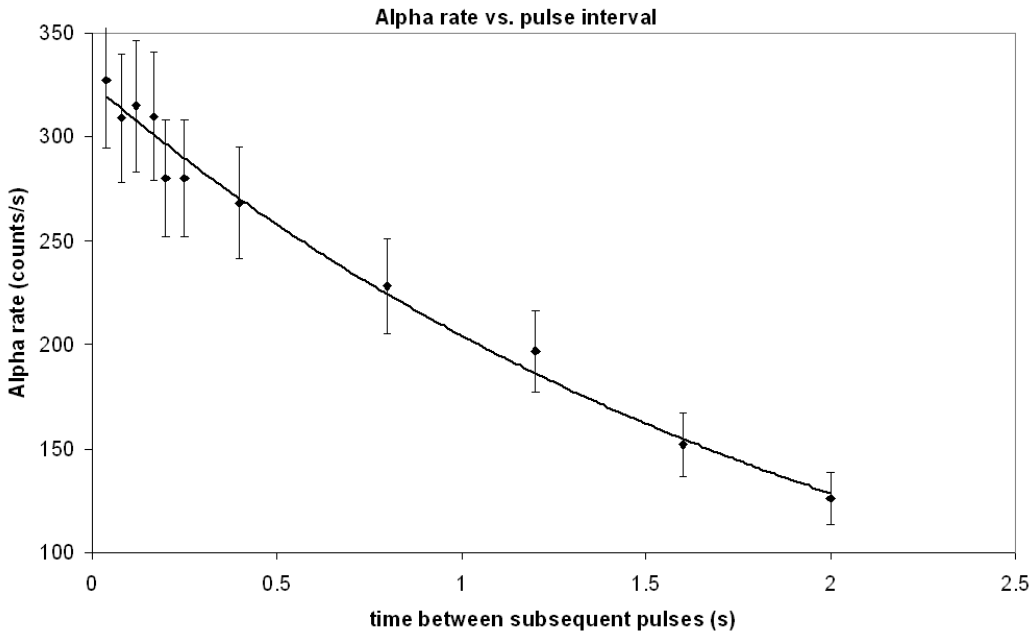

Figure 5.8: The alpha rate and the pulse intervals are related exponentially. Longer wait times in the trap result in decrease in alpha rate.

trapped in the first RFQ structure. We keep the first trap "closed" for some time and we "open" the trap again to pulse the ion bunch out. The time between two subsequent pulses and the corresponding alpha rate at our detector is shown in Figure 5.8. Apparently, more ions are lost the longer we wait. For this particular incoming Fr^+ beam intensity (327 counts per second for 40ms pulse interval), the half-life of the trap is found to be $t_{1/2} = 1.49s$.

The next set of data is taken with a lower intensity Fr^+ beam. By changing the cone voltage, the beam is defocused for lower intensity (104 counts per second for 40ms pulse intervals). Again, the relationship between the pulse interval and alpha rate is recorded (see figure 5.9). For this particular case, the half-life of the trap is calculated to be $t_{1/2} = 6.82s$. This means that, as

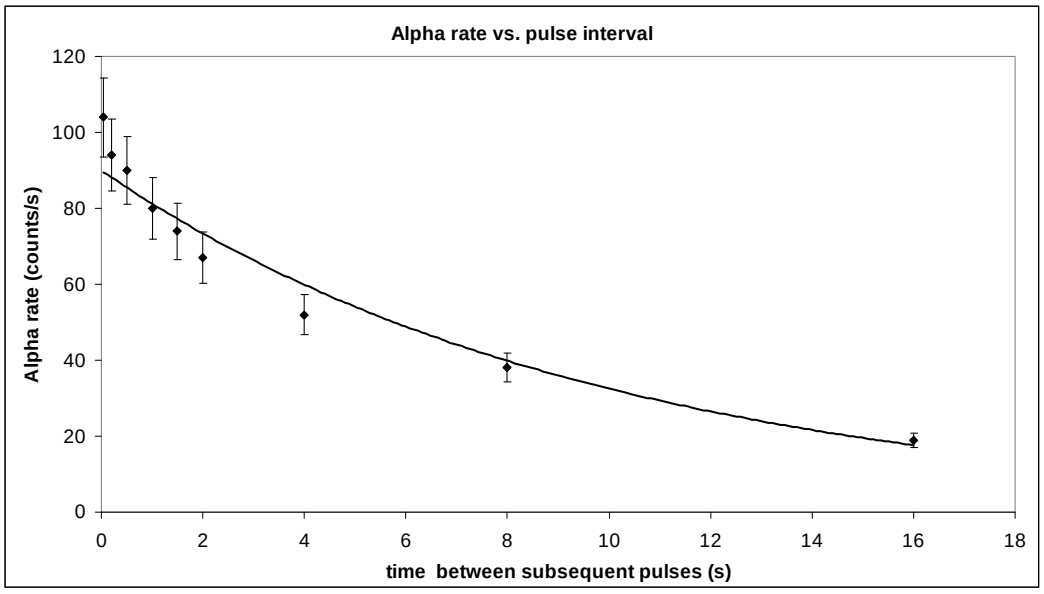

Figure 5.9: As the beam intensity gets lower, the ions can stay in the trap for longer periods of time.

the number of Fr^+ ions in the trap increases, the lifetime of the trap decreases, i.e. the ions are lost at a higher rate when the number of ions in the trap is high.

The trap lifetime may depend on the number of ions in the trap for various reasons. One is the space-charge effect. To have an idea about the strength of this effect, we can treat the trapped ions as a cloud of radius r. Then the potential at the surface of this cloud can be approximated by Gauss's law, $V = \frac{1}{4\pi\varepsilon_0}\frac{Q}{r}$ where Q is the total charge in the cloud. The number of Fr ions that reach to our detector was of the order of $10^3/s$. Assuming a lower limit of 1% for the transmission efficiency from the first trap to the detector, a solid angle of 6% for the detector and a trap radius of $r = 3$ mm, we find $V \approx 0.8$ Volts. The trap creates a DC potential well of 15 V in the axial direction by

applying DC voltages to the segments and a pseudo-potential of 22.3 V, which is calculated using (2.46) for the Fr trapping parameters; *i.e* RF voltage = 500 V, $r_0 = 7.85$ mm, $\omega = 2\pi(725$ kHz). So the space-charge effect is too small to account for the change in trap lifetime at Fr intensities shown in Figures 5.8 and 5.9.

The collisions between the Fr ions and the background He buffer gas are unlikely to create a change in trap lifetime, since we have the same He pressure for both intensities. Because the rate dropped with increasing Fr density, then one possibility is $Fr^+ - Fr^+$ collisions knocking atoms out of the trap. Further work is needed to investigate this process in detail.

Chapter 6

g-Factor Measurements: A Proposed Method

So far we have discussed the trapping conditions for ion beams, which is the main focus of this dissertation. As introduced in Chapter 1, the goal of this experiment is to make precise nuclear g-factor measurements in Francium isotopes. To be able to do such measurements, we should also consider the sections of our beamline we constructed (shown in Figure 1.1) other than the trapping region. In this chapter, I will introduce other mechanisms related to a g-factor measurement. These mechanisms are discussed in detail in Jerry Sell's Ph.D dissertation [21].

6.1 Collinear Laser Spectroscopy

After Fr is extracted out of the gold target as Fr^+, the ions travel between the two deflecting electrodes with voltages applied to them. This gives the

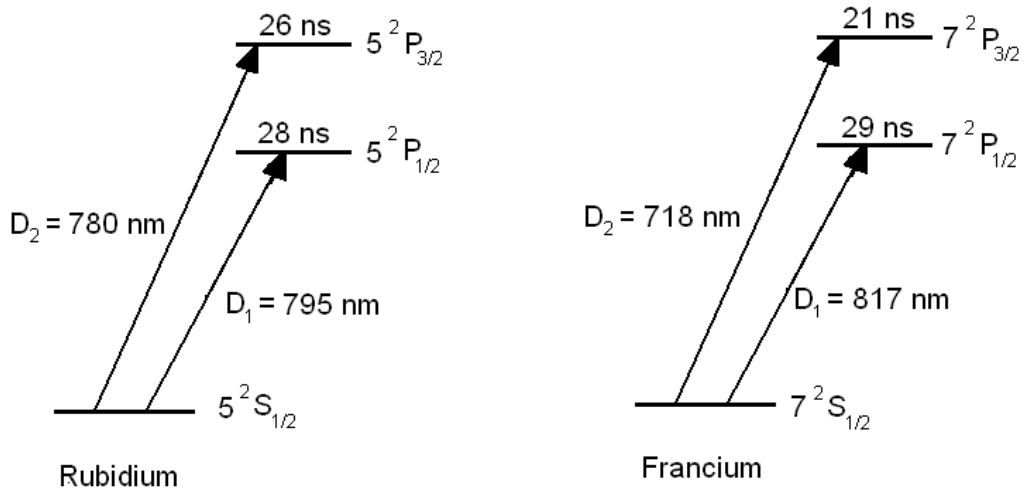

Figure 6.1: Enery levels and lifetimes of basic atomic states used in optical pumping of Rb and Fr.

ions a 10^o bend, to allow the laser beam to enter coaxial to the ion beam as shown in Figure 1.1. To keep the energy spread and astigmatism of the beam minimum, the angle is selected smallest possible. The ions, which are then focused on the tungsten ionizer, are analyzed using the collinear spectroscopy methods by Jerry Sell, on their way to the ionizer. Unlike the large intensity Rb beams, the atomic resonance signal for small Fr beam intensities in our case is very difficult to distinguish from the background signal. Much effort has been put to minimize the background scattering light from the Fr beam. The energy levels and lifetimes used in optical pumping of Fr are given in figure 6.1. We already had the necessary laser equipment from earlier MOT experiments of the francium group. The laser beam is brought by optical fibers to the experimental area.

6.2 Rubidium Jet Neutralizer

To use the optical pumping method for polarizing Fr, we have to neutralize the Fr^+ ions. A charge-exchange reaction, where an electron is transferred, takes place between the two interacting species.

$$A^0 + B^+ \rightarrow A^+ + B^0 + \Delta E \tag{6.1}$$

ΔE is called the energy defect. It is the change in internal energy of the system. ΔE is zero when A and B are same species. ΔE has to be close to zero for an efficient charge exchange. ΔE in the reaction between Fr^+ and Rb^0 is 0.1 eV, lowest compared to Fr^+ reacting with other alkalis. So a clever choice of neutralizing vapor would be Rb vapor, since in our case we do not have Fr vapor available. The charge exchange cross-section for Fr^+ and Rb^0 is estimated to be $10^{-14} - 10^{-15}$ cm^2 [21]. We have developed a neutralizer model similar to the one used in TRIUMF [29] and BNL [30]. The diagram of the rubidium jet neutralizer is shown in Figure 6.2.

We have a Rb reservoir at the bottom of the apparatus where we place a small (5gr) Rb ampoule. We keep the reservoir and the thicker flow pipe at $\sim 200^0$C which makes the Rb flow upward towards the neutralization chamber, because of the pressure difference between the reservoir and neutralization chamber. The nozzle helps us to have a strong jet-type flow. The temperature of the neutralization chamber is measured to be $\sim 130^0$C. The relative coolness of the return path keeps the upward Rb flow through the thinner pipe low. A 90% Fr^+ neutralization rate was achieved with about 220^0C at the reservoir.

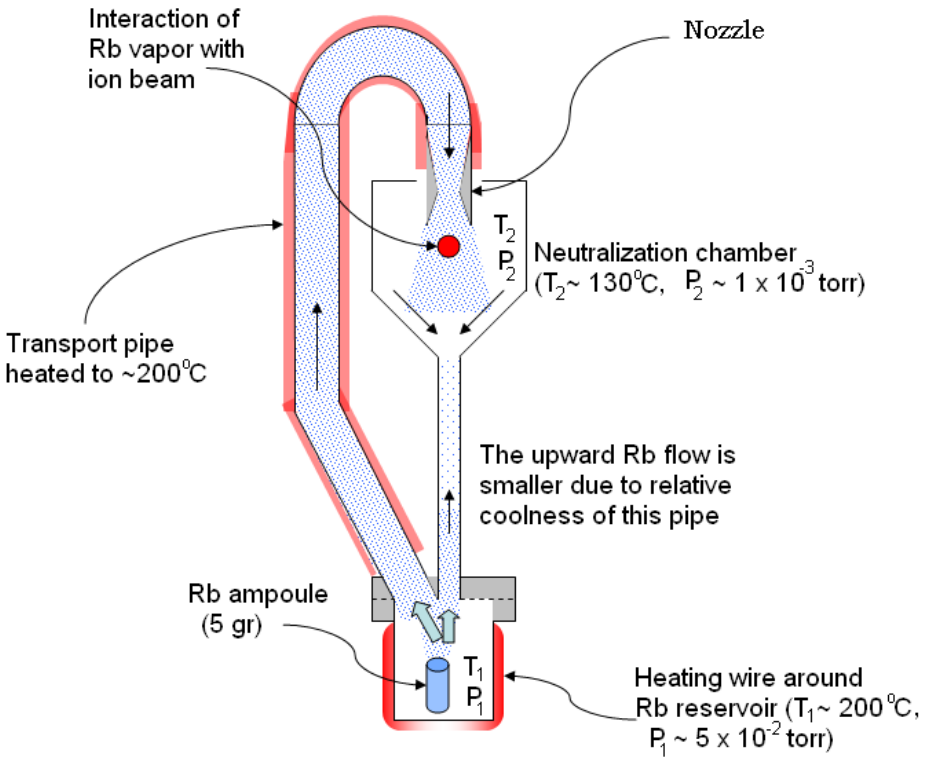

Figure 6.2: Diagram of the Rb jet neutralizer (figure taken from [21]).

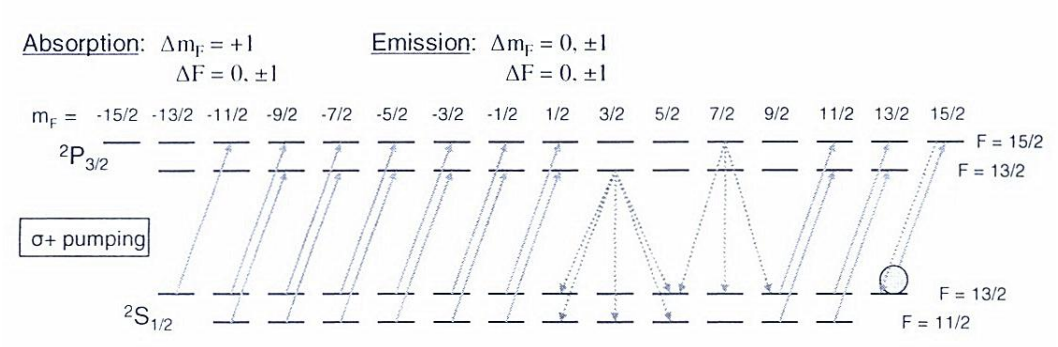

Figure 6.3: The magnetic sublevels of ^{210}Fr optically pumped with $\sigma+$ polarizing light (figure taken from [21]).

6.3 Optical Pumping to Polarize Atoms

To bring the neutral Fr atoms into a polarization state, an optical pumping method was planned. The magnetic sublevels of ^{210}Fr optically pumped with $\sigma+$ light are shown in Figure 6.3.

With no pumping light and in the absence of a magnetic field, the atoms are highly populated in the $^2S_{1/2}$ state, and equally distributed among all magnetic sublevels for a given hyperfine level. To define the magnetic quantization axis, a small magnetic field ($\sim$ 10 Gauss) can be applied along the beam axis. The circularly polarized $\sigma+$ light stimulates the atom to gain $\Delta m_F = +1$. Spontaneous emission occurs with $m_F = 0, \pm 1$. So after sufficient cycles of optical pumping on both ground state hyperfine levels to achieve a higher polarization efficiency, most of the atoms will occupy the highest m_F state.

6.4 The Re-ionization and Preserving Polarization

The polarized neutral beam will reach the tungsten ionizer, where Fr leaves the hot surface of the ionizer as a positive ion. Stopping the ions there also enables us to reduce the kinetic energies of the ions from 5keV to about 100eV, provided the potential of the ionizer is kept at 100V. A rather difficult task is preserving the nuclear polarization state. Our method relies on the work by Fick *et al.* where they investigated the nuclear polarization preservation on ^{6}Li and ^{23}Na landing on hot metal surfaces [20]. They found that when the ionized particles are under a magnetic field sufficiently high to decouple the electronic and nuclear angular momenta, they preserve their polarization state for a tungsten surface temperatures of $\sim 1100^{o}$C. The polarization preservation can be expressed as

$$P(T) = \frac{P_0}{\alpha\tau} \tag{6.2}$$

where P_0 is the polarization of the incoming atomic beam, τ is the mean residence time on the surface, and α is the polarization relaxation, which is a function of the temperature, and was found to be $2-3\ s^{-1}$, for alkali atoms on a tungsten surface [31]. The tungsten ionizer assembly fits into a 2" diameter beam pipe, which will fit into the bore of an electromagnet. The magnet, from Arnold Magnetic Technologies, which can produce magnetic fields of about 0.8T, was tested by an undergraduate student. This strength of magnetic field is enough to reach the strong-field limit (Paschen-Bach region) for Rb, but Fr needs ~ 1.5 T to reach to that limit. Because the fraction of polarized atoms

decreases at magnetic fields lower than this limit, we foresee a loss in the polarization preservation rate, which can be partially compensated by having the tungsten surface at higher temperatures, thus decreasing the residence time of the atom on the surface. We have a working system of surface ionization, and a tested magnet, which needs to be installed on the ionization region when we try the optical pumping.

6.5 Nuclear g-factor measurement

After the ions are confined in the longer trap, the ions are then extracted and transferred into the shorter trap, as discussed in earlier chapters. The second trap will have a pair of RF coils inside its cubical housing. The polarized ions in the trap will emit alpha particles preferentially in a particular direction with respect to an applied magnetic field. The RF coils can be used to induce Zeeman transitions among the 2I+1 nuclear sublevels. The frequency ν is related to g_I by

$$h\nu = g_I \mu_N B_{ext} \tag{6.3}$$

The anisotropy in the trapped ions will be destroyed by the RF magnetic field when the field corresponds to the Zeeman splitting. It is important to have the trap size small, giving the smallest possible magnetic inhomogeneity, to have a precise g-factor determination.

6.6 Conclusions

Our group has so far built an operational collinear spectroscopy system, and a tested high quality magnetic field system, so the polarization is in principle possible. Also, the transport of the ions from the tungsten ionizer to the end of the system is demonstrated. Successful trapping conditions for Rb in both traps are established. Some of the trapping parameters for Fr have also been determined, but the transmission efficiency in the ejection of the Fr ions from the long trap and in catching them by the short trap needs to be improved. Because of the low available intensity of Fr beam, any improvement in transmission efficiency is important. We have also shown that the real-life working parameters for Fr trapping are consistent with the theory of ion traps, and that our RFQ guide can be used as an ion separator to separate the Fr ions from the Rb ions, which are abundant in our system because of the use of Rb vapor as a neutralizer gas. Measurements on the trap lifetime for Fr ions were performed to better understand their behavior in a trap.

Francium studies open up a wide variety of possibilities in nuclear structure and weak interaction studies, and in performing precision measurements to test the atomic theory. A great proportion of the apparatus for g-factor measurements on Fr is now ready. However Fr production is currently unavailable at Stony Brook and the project will possibly move to another facility.

Bibliography

[1] Wood C. S., Bennett S. C., Cho D., Masterson B. P., Roberts J. L., Tanner C. E. and Wieman C. E.; Science **275**, 1759 (1997)

[2] Wood C. S., Bennett S. C., Roberts J. L., Cho D. and Wieman C. E.; Can. J. Phys. **77**, 7 (1999)

[3] Blundell S. A., Johnson W. R. and Sapirstein J.; Phys. Rev. A **43**, 3407 (1991)

[4] Dzuba V. A., Flambaum V. V. and Sushkov O. P.; Phys. Lett. A **141**, 147 (1989)

[5] Langacker P.; Precision Tests of the Standard Electroweak Model (World Scientific, Singapore) (ed: 1995)

[6] Erler J. and Langacker P.; Phys. Rev. Lett. **84**, 212 (2000)

[7] Safranova M. S. and Johnson M. R.; Phys.Rev. A **62**, 022112 (2000)

[8] Perey M.: C. R. Acad. Sci. **208**, 97 (1939)

[9] Liberman S., Pinard J., Duong H. T., Juncar P., Vialle J. L., Jacquinot P., Huber G., Touchard F., Büttgenbach S., Pesnelle A., Thibault C.,

Klapish R. and the ISOLDE Colloboration; C. R. Acad. Sci. B **286**, 253 (1978)

[10] Lide E. D. R.; CRC Handbook of Chemistry and Physics, 75^{th} ed. (CRC Press, Boca Raton) (1994)

[11] Lu Z. T., Corwin K. L.,Vogel K. R., Wieman C. E., Dinneen T. P., Maddi J. and Gould H.; Phys. Rev. Lett. **79**, 994 (1997)

[12] Andreev S. V., Mishin V. I. and Letokhov V. S.; J. Opt. Soc. Am. B **5**, 2190 (1988)

[13] Simsarian J. E., Ghosh A., Gwinner G., Orozco L. A., Sprouse G. D. and Voytas P. A.; Phys. Rev. Lett. **76**, 3522 (1996)

[14] Aubin S., Gomez E., Orozco L. A. and Sprouse G. D.; Rev. Sci. Instr. **74**, 4342 (2003)

[15] Gomez E., Orozco L. A. and Sprouse G. D.; Rep. Prog. Phys. **69**, 79 (2006)

[16] Flambaum V. V., Khriplovich I. B. and Sushkov O. P.; Phys. Lett. B **146**, 367 (1984)

[17] Grossman J. S., Orozco L. A., Pearson M. R., Simsarian J. E., Sprouse G. D. and Zhao W. Z.; Phys. Rev. Lett. **83**, 935 (1999)

[18] Coc A., Thibault C., Touchard F., Duong H. T., Juncar P., liberman S., Pinard J., Lermé J., Vialle J. L., Büttgenbach S., Mueller A. C., Pesnelle A. and the ISOLDE Colloboration; Phys. Lett. B **163B**, 66 (1985)

[19] Bohr A. and Weisskopf V. F.; Phys.Rev. **77**, 94 (1950)

[20] Beckmann E., Horn B. and Fick D.; Z. Phys. B **48**, 335 (1982)

[21] Sell J. F; Ph.D. Thesis, (Stony Brook University) (2007)

[22] Paul W., Steinwedel H.; RZeitschrift für Naturforschung A, **8**, 448 (1953)

[23] Dawson P.H.; Quadrupole Mass Spectrometry and its Applications (Elsevier, Amsterdam) (1976)

[24] Dineen T., Ghiorso A. and Gould H.; Rev. Sci. Instrum. **67**, 752 (1996)

[25] Dayton I. E., Shoemaker F. C. and Mosley R. F.; Rev. Sci. Instrum. **25**, 485 (1954)

[26] Denison D. R.; J. Vac. Sci. Technol. **8**, 266 (1971)

[27] Dahl D. A.; SIMION 3D ver.7.0, (Scientific Istrument Services, Ringoes, NJ) (2000)

[28] Ziegler J. F.; SRIM - The Stopping and Range of Ions in Matter Software, (2000) http://www.srim.org/

[29] Levy C. D. P.' Baartman R., Jayamanna K., Kiefl R., Kuo T., Olivio M., Wight G. W., Yuan D. and Zelenski A. N.; Nucl. Phys. A **701**, 253c (2002)

[30] Zelenski A. N.; AIP Conf. Proc. **570**, 179 (2001)

[31] Wassmuth K. and Fick D.; Phys. Rev. Lett. **59**, 3007 (1987)